

Earth's early continental crust formed from wet and oxidizing arc magmas

<https://doi.org/10.1038/s41586-023-06552-0>

Rong-Feng Ge¹✉, Simon A. Wilde², Wen-Bin Zhu¹ & Xiao-Lei Wang¹

Received: 6 December 2022

Accepted: 17 August 2023

Published online: 27 September 2023

 Check for updates

Formation of continental crust has shaped the surface and interior of our planet and generated the land and mineral resources on which we rely. However, how the early continental crust of Earth formed is still debated^{1–7}. Modern continental crust is largely formed from wet and oxidizing arc magmas at subduction zones, in which oceanic lithosphere and water recycle into the mantle^{8–10}. The magmatic H₂O content and redox state of ancient rocks that constitute the early continental crust, however, are difficult to quantify owing to ubiquitous metamorphism. Here we combine two zircon oxybarometers^{11,12} to simultaneously determine magmatic oxygen fugacity ($f\text{O}_2$) and H₂O content of Archaean (4.0–2.5 billion years ago) granitoids that dominate the early continental crust. We show that most Archaean granitoid magmas were ≥ 1 log unit more oxidizing than Archaean ambient mantle-derived magmas^{13,14} and had high magmatic H₂O contents (6–10 wt%) and high H₂O/Ce ratios (>1,000), similar to modern arc magmas. We find that magmatic $f\text{O}_2$, H₂O contents and H₂O/Ce ratios of Archaean granitoids positively correlate with depth of magma formation, requiring transport of large amounts of H₂O to the lower crust and mantle. These observations can be readily explained by subduction but are difficult to reconcile with non-subduction models of crustal formation^{3–7}. We note an increase in magmatic $f\text{O}_2$ and H₂O content between 4.0 and 3.6 billion years ago, probably indicating the onset of subduction during this period.

The exposed early continental crust on Earth is mainly composed of Archaean granitoids dominated by tonalite, trondhjemite and granodiorite (TTG), with subordinate volcanic and sedimentary rocks^{15,16}. Deciphering the formation conditions of TTG magmas is therefore key to understanding the origin of continental crust and prevailing geodynamic regimes on the early Earth. TTG magmas can be produced by either partial melting of hydrated basalts or fractionation of hydrous basaltic to intermediate magmas^{15,16}. Most Archaean TTGs have trace-element patterns (for example, depletion of heavy rare-earth elements (HREE)) that suggest formation at depths at which garnet is stable, corresponding to ≥ 0.7 –0.8 GPa (refs. 5,15,16). However, in what tectonic environment Archaean TTGs formed remains highly contentious. Both subduction-related^{1,2} and various non-subduction models^{3–7} have been proposed. The latter mostly predict a stagnant-lid tectonic regime characterized by large-scale volcanism and vertical tectonism^{3–6}, probably punctuated by giant impacts⁷. Previous studies have largely focused on geochemical diversity of TTGs and its implications for source compositions and formation depths of TTG magmas^{15,16}, whereas other variables that may play an important role during magma formation remain largely unexplored.

Magmatic oxygen fugacity ($f\text{O}_2$) and H₂O content are two critical variables that govern magma generation, differentiation and mineralization^{8–10}. On the modern Earth, arc magmas formed at subduction zones are characterized by high $f\text{O}_2$ and H₂O contents, largely because of the

influx of oxidizing fluids released from subducting oceanic plates^{8–10}. Such wet and oxidizing arc magmas are the primary building block of modern continental crust^{8–10}. Therefore, determining magmatic $f\text{O}_2$ and H₂O contents of Archaean igneous rocks is vital to testing how the early continental crust was formed. However, quantifying magmatic $f\text{O}_2$ and H₂O content of these ancient rocks is difficult. The commonly used methods, including direct measurement of Fe³⁺/ΣFe ratios and H₂O content in melt inclusions^{8–10} and estimates based on mineral–melt equilibria¹⁷, are rarely applicable to Archaean rocks, simply because melt inclusions are rare or absent, and the primary minerals may have been modified by metamorphism. Recent studies of olivine-hosted melt inclusions in well-preserved Archaean komatiites reveal an H₂O-rich mantle transition zone formed by recycling of oceanic lithosphere before 3.3 billion years ago (Ga)^{18,19}, whereas the V/Sc (ref. 13) and V/Ti (ref. 14) ratios of Archaean basalts suggest that the Archaean ambient mantle might have been ≥ 1 log unit more reducing than its modern counterpart. However, the magmatic $f\text{O}_2$ and H₂O content of the dominant granitoids remain largely unknown.

Azircon oxybarometer-hygrometer

Zircon is a robust mineral that is able to preserve magmatic compositions even in ancient rocks that experienced high-grade metamorphism and partial melting. Recently, several oxybarometers based

¹State Key Laboratory for Mineral Deposits Research, Institute of Continental Geodynamics, Frontiers Science Center for Critical Earth Material Cycling, School of Earth Sciences and Engineering, Nanjing University, Nanjing, People's Republic of China. ²The Institute for Geoscience Research, School of Earth and Planetary Sciences, Curtin University, Perth, Western Australia, Australia.  e-mail: gerongfeng@nju.edu.cn

on zircon composition have been proposed^{11,12}. Here we introduce a magma hygrometer based on a combination of the $\text{Ce}^{4+}/\text{Ce}^{3+}$ oxybarometer¹¹ and the Ce-U-Ti oxybarometer¹². The former was established on the basis of experimental results²⁰ and is sensitive to equilibrium melt composition, especially H_2O content, whereas the latter is empirically calibrated and is independent of the equilibrium melt composition. For a given equilibrium zircon–melt composition, the $\text{Ce}^{4+}/\text{Ce}^{3+}$ oxybarometer¹¹ establishes that the magmatic $f\text{O}_2$ and H_2O contents are positively correlated, so the magmatic H_2O content can be calculated from $f\text{O}_2$ values obtained using the independent Ce-U-Ti oxybarometer¹² (Fig. 1a; Methods). A test using magmatic suites with well-known H_2O contents shows that this zircon oxybarometer-hygrometer can retrieve the median magmatic H_2O contents during zircon crystallization in Archaean to modern magmas from various tectonic settings within 1 weight per cent (wt%) uncertainty (inset in Fig. 1a; Methods).

$f\text{O}_2$ and H_2O of Archaean granitoid magmas

Using the zircon oxybarometer-hygrometer established above, we calculated magmatic $f\text{O}_2$ and H_2O content for Archaean granitoids worldwide (Extended Data Fig. 1) based on new and published zircon and whole-rock compositional data (Supplementary Tables 1–3; Methods). Similar data for rare Archaean^{21,22} and typical Mesozoic–Cenozoic^{23,24} granitoids associated with porphyry Cu ± Au ± Mo deposits (PCDs), as well as detrital Hadean zircons from the Jack Hills (Australia)^{25,26}, were also compiled for comparison. All the data were filtered using the same criteria to extract primary magmatic compositions^{25,27} (Methods).

The results (Figs. 1b and 2 and Supplementary Table 3) show that most Archaean granitoids have magmatic $f\text{O}_2$ within 1 log unit of the fayalite–magnetite–quartz (FMQ) buffer (median FMQ -0.1 ± 1.1 , 2 s.d.), which are significantly more reducing than Phanerozoic arc magmas (median FMQ $+1.4 \pm 1.1$, 2 s.d.)^{8,9} and granitoids associated with PCDs (median FMQ $+1.9 \pm 0.9$, 2 s.d.). However, compared with recent estimates of the $f\text{O}_2$ of Archaean ambient mantle-derived magmas^{13,14}, the $f\text{O}_2$ of most Archaean granitoid magmas is ≥ 1 log unit higher. This increase of $f\text{O}_2$ is similar to that in Phanerozoic arc magmas relative to contemporary ambient mantle-derived magmas^{8,9}. However, the 4.02–3.75-Ga gneisses in the Acasta complex, which represent some of the oldest rocks on Earth^{28,29}, record significantly lower $f\text{O}_2$ (median FMQ -1.8 to -2.0), indicating the more reducing nature of the parental magmas. Most detrital zircons from the Jack Hills record broadly similar $f\text{O}_2$ to Archaean TTG zircons, but there is also a significant proportion (about 37%) of more reduced values ($\text{FMQ} < -1$) in grains older than 3.8 Ga (Supplementary Table 1).

The zircon oxybarometer-hygrometer yields magmatic H_2O contents ranging from 3.9 to 10.5 wt% for individual Archaean granitoids (Figs. 1b and 2e–h and Supplementary Table 3). This demonstrates the diversity of Archaean granitoids, from which three groups can be recognized. Group 1 granitoids (such as the 4.02–3.75-Ga Acasta gneisses) have relatively low H_2O (3.9–4.6 wt%), consistent with their less evolved and Fe-rich compositions^{28,29}. Group 2 granitoids (such as those from Yilgarn^{22,23}) have moderate H_2O contents (6.0–6.4 wt%), similar to those of Phanerozoic subduction-related felsic volcanic rocks (such as the Bishop and Toba tuffs). Group 3 granitoids (such as the 3.56-Ga Acasta gneisses^{28,29} and the 3.72-Ga Aktash gneisses^{30,31}) have very high magmatic H_2O (8.1–10.5 wt%), similar to those of Phanerozoic granitoids associated with PCDs, as estimated using the same method (8.0–8.8 wt%) and inferred independently from phase relations²⁴. Similarly high magmatic H_2O contents are also obtained for evolved rocks associated with Archaean PCDs^{21,22}. The parental magmas of the detrital Hadean zircons from the Jack Hills remain elusive and, assuming a variety of source rocks, their model H_2O contents range from 4.2 to 8.5 wt%, with median values (4.5–5.6 wt%) similar to those obtained for the 4.02-Ga Acasta rocks.

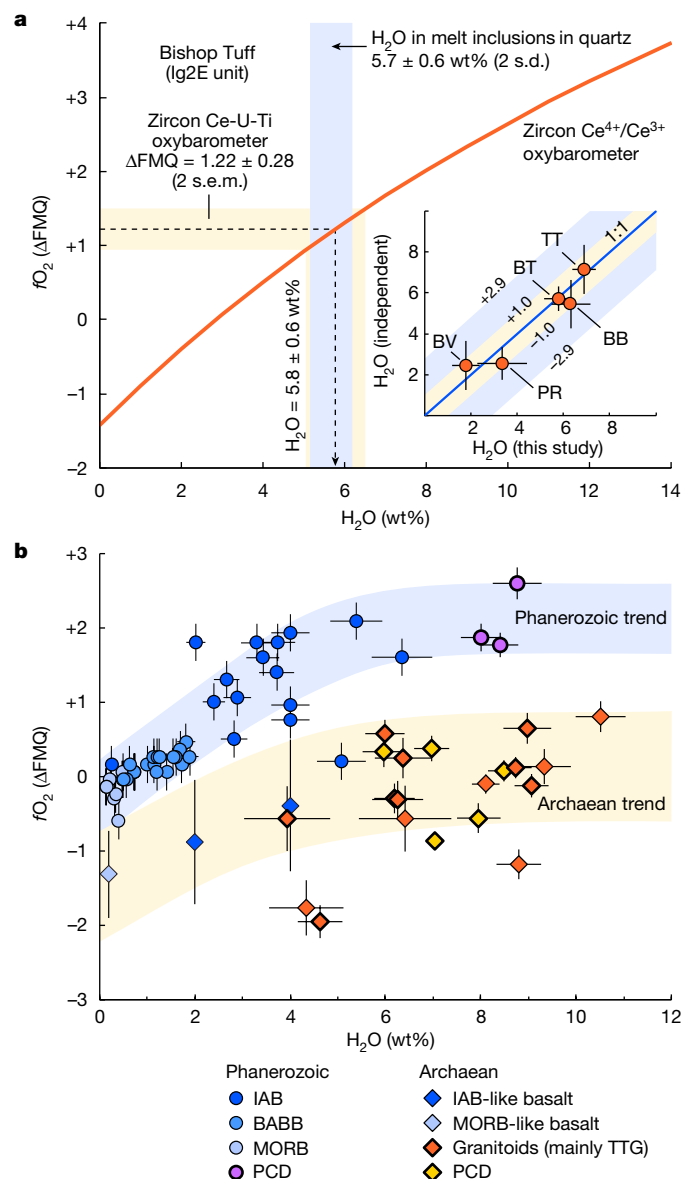


Fig. 1 | The principle of the zircon oxybarometer-hygrometer. **a**, The relationship (orange curve) between magmatic H_2O content and $f\text{O}_2$ relative to the FMQ buffer (ΔFMQ) according to the zircon $\text{Ce}^{4+}/\text{Ce}^{3+}$ oxybarometer¹¹ for the Ig2E unit of the Bishop Tuff (California). The dashed line shows the median ΔFMQ value according to the zircon Ce-U-Ti oxybarometer¹² and the corresponding H_2O content. The blue bar shows the magmatic H_2O content in quartz-hosted melt inclusions⁴⁴. The inset shows a comparison of the magmatic H_2O content estimated using the zircon oxybarometer-hygrometer (this study) and independent techniques for the Bushveld Complex (BV)⁴⁵, Pea Ridge tuff (PR)⁴⁶, Bishop Tuff (BT)⁴⁴, Younger Toba Tuff (TT)¹⁷ and Barberton mafic-ryholite (BB)⁴⁷ (Supplementary Table 3). Although the zircon oxybarometer-hygrometer has a total uncertainty of about 2.9 wt% for individual zircon–whole-rock/melt analyses (blue bands in the inset; see Methods), it reproduces the median H_2O contents within 1 wt% uncertainty (yellow bands in the inset). **b**, Results of the zircon oxybarometer-hygrometer (orange, yellow and purple symbols). Symbols with heavy and light outlines show data uncorrected and corrected for U loss, respectively (see Methods and Extended Data Fig. 2). Melt inclusion data for Phanerozoic mid-ocean ridge basalt (MORB), back-arc basin basalt (BABB) and island arc basalt (IAB)^{8,9}, as well as $f\text{O}_2$ of MORB-like and IAB-like Archaean basalts estimated using V/Ti ratios¹⁴, are also shown for comparison. The blue and yellow bands show the increase in $f\text{O}_2$ and H_2O in the Phanerozoic and Archaean magmas, respectively, relative to contemporaneous ambient mantle-derived MORB-like magmas. Error bars are 2 s.e.m. for the zircon oxybarometer-hygrometer results, 10% for H_2O content and 0.25 log units for $f\text{O}_2$ for Phanerozoic melt inclusion data, and 1 s.d. for $f\text{O}_2$ of Archaean basalts.

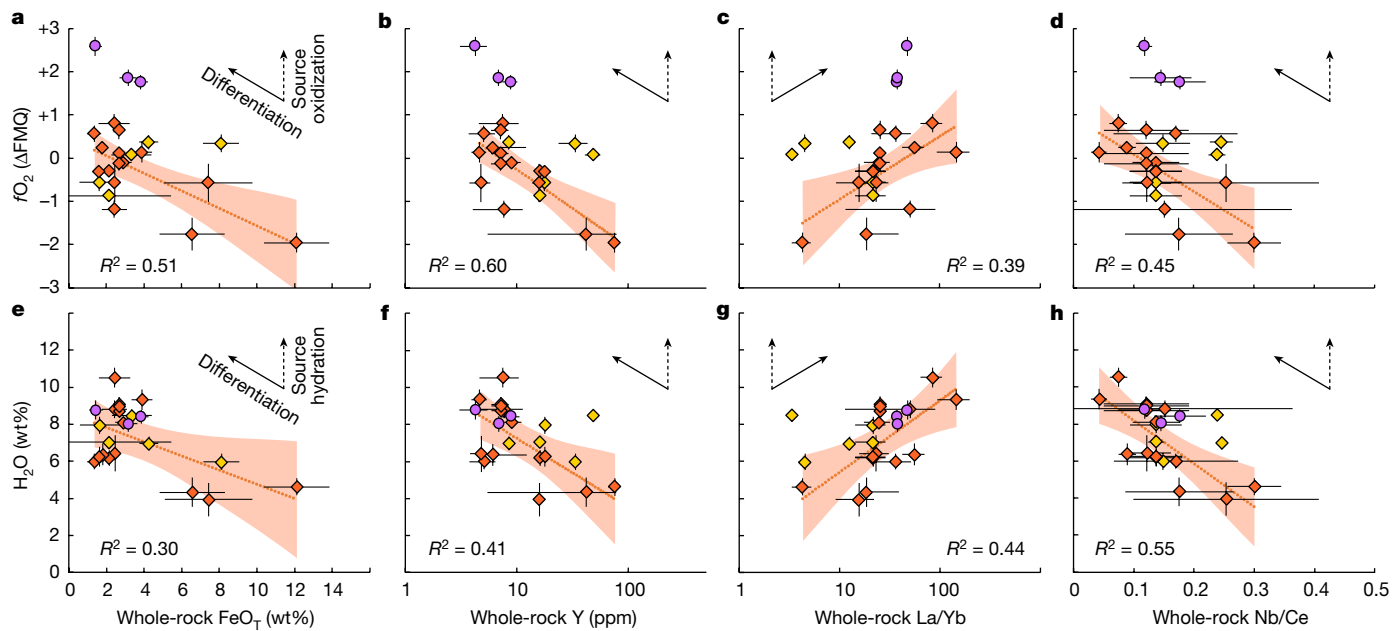


Fig. 2 | Magmatic $f\text{O}_2$ and H_2O contents correlate with whole-rock compositions. **a–d**, Correlations of magmatic $f\text{O}_2$ relative to the FMQ buffer (ΔFMQ) with whole-rock compositions. **e–h**, Correlations of magmatic H_2O content with whole-rock compositions. FeO_T , total Fe expressed as FeO . See Extended Data Fig. 3 for correlations with other elements and ratios. Median values are used in the plots (Supplementary Table 3). Error bars are 2 s.e.m. Dotted orange lines show regressions for Archaean granitoids (orange diamonds) and the shaded areas are 95% confidence intervals. Data for

Archaean (yellow diamonds) and Phanerozoic (purple circles) granitoids associated with PCDs are also plotted for comparison. R , correlation coefficient. The solid and dashed arrows show the expected trends for deep magma differentiation and source oxidation/hydration, respectively. Note that Phanerozoic and some Archaean granitoids associated with PCDs have higher $f\text{O}_2$ at similar degrees of differentiation, consistent with the role of high $f\text{O}_2$ in the formation of such deposits, as well as secular oxidization of crustal magmas and the mantle^{13,14}.

Thermodynamic-geochemical constraints

Our results provide the first quantitative constraints on magmatic $f\text{O}_2$ and H_2O contents of Archaean granitoids worldwide and highlight the diverse but generally H_2O -rich and oxidizing nature of their parental magmas relative to Archaean ambient mantle-derived magmas^{13,14}. The $f\text{O}_2$ and H_2O contents recorded by the zircon oxybarometer-hygrometer are mainly controlled by three processes: (1) magma crystallization; (2) magma formation; and (3) source oxidation and hydration. We carried out detailed thermodynamic-geochemical modelling to 'see through' these processes (Methods).

Our modelling indicates that magmatic $f\text{O}_2$ decreases by at least 0.6–0.8 log units when zircon crystallizes in hydrous TTG magmas (process 1; Fig. 3a and Extended Data Fig. 6c,d), because ilmenite and amphibole that crystallize earlier have slightly higher $\text{Fe}^{3+}/\Sigma\text{Fe}$ ratios than the primary TTG melts. This is supported by the negative correlation between zircon Hf contents and $f\text{O}_2$ in several TTG suites (Extended Data Fig. 4). The implication is that the median $f\text{O}_2$, and therefore H_2O contents, obtained above are probably minimum estimates for the primary magmas, supporting the relatively oxidizing and H_2O -rich nature of most Archaean granitoid magmas.

Magma crystallization (process 1) also drives H_2O enrichment in H_2O -undersaturated systems, so that high magmatic H_2O can be achieved in highly evolved magmas (path A in Fig. 3a and Extended Data Fig. 6c,d). However, if this were the case, our modelling predicts a negative correlation between magmatic H_2O and $f\text{O}_2$, which is opposite to the broadly positive correlations observed in several TTG suites (for example, Acosta and Barberton) as well as in the global dataset (Fig. 1b). Alternatively, the distinct magmatic H_2O contents in Archaean granitoids can be explained by zircon crystallization in H_2O -saturated magmas at different depths (0.2–0.5 GPa; path B in Fig. 3a and Extended Data Fig. 6c,d), which are controlled by primary magmatic H_2O contents³². We conclude that magma crystallization is not the primary

mechanism determining different $f\text{O}_2$ and H_2O in Archaean granitoid magmas obtained above.

By contrast, we find that the magmatic $f\text{O}_2$ and H_2O of Archaean granitoids correlate with whole-rock geochemical indexes of magma differentiation and depth of magma formation (Fig. 2 and Extended Data Fig. 3). Although the estimate of magmatic H_2O content is dependent on the whole-rock composition, the zircon Ce-U-Ti oxybarometer¹² is not, indicating that these correlations are not artefacts. Instead, these observations can be explained by high-pressure fractionation of garnet³³. Garnet contains high Fe, HREE and Y, but low SiO_2 and Fe^{3+} , so that its fractionation drives simultaneous depletion of Fe, HREE and Y and enrichment of SiO_2 , H_2O and Fe^{3+} , thereby increasing the $\text{Fe}^{3+}/\Sigma\text{Fe}$ ratio and $f\text{O}_2$ of the evolving magmas³³. The correlations of $f\text{O}_2$ and H_2O with whole-rock Nb/Ce and TiO₂ (Fig. 2d,h and Extended Data Fig. 3) indicate that rutile also plays a role, consistent with high-pressure differentiation. Our modelling demonstrates that increasing pressure of magma formation (process 2) can explain simultaneous H_2O enrichment and oxidization of the resultant TTG melts (path C in Fig. 3b).

However, our modelling in the P – H_2O and P – $f\text{O}_2$ spaces (Fig. 3c,d) indicates that garnet fractionation from Archaean ambient mantle-derived mafic magmas is unable to produce the highest H_2O and $f\text{O}_2$ (about 10 wt% and $\Delta\text{FMQ} > 0$) observed in Archaean granitoids. This is because: (1) the H_2O contents of ambient mantle-derived magmas are generally very low (<0.5 wt%)^{8–10}, so that even extreme differentiation cannot generate melts with approximately 10 wt% H_2O (path D in Fig. 3c) and (2) the garnet effect in increasing $f\text{O}_2$ is buffered to less than 1 log unit by coexisting clinopyroxene and, to a lesser extent, amphibole, both of which have higher $\text{Fe}^{3+}/\Sigma\text{Fe}$ ratios than TTG melts under most conditions. Instead, the relatively enriched, oxidizing and H_2O -rich mafic rocks/magmas^{14,30}, presumably derived from interaction with H_2O either in their mantle source or at the sea floor on eruption, seem to be appropriate sources for Archaean TTGs (paths E–I in Fig. 3c,d). The

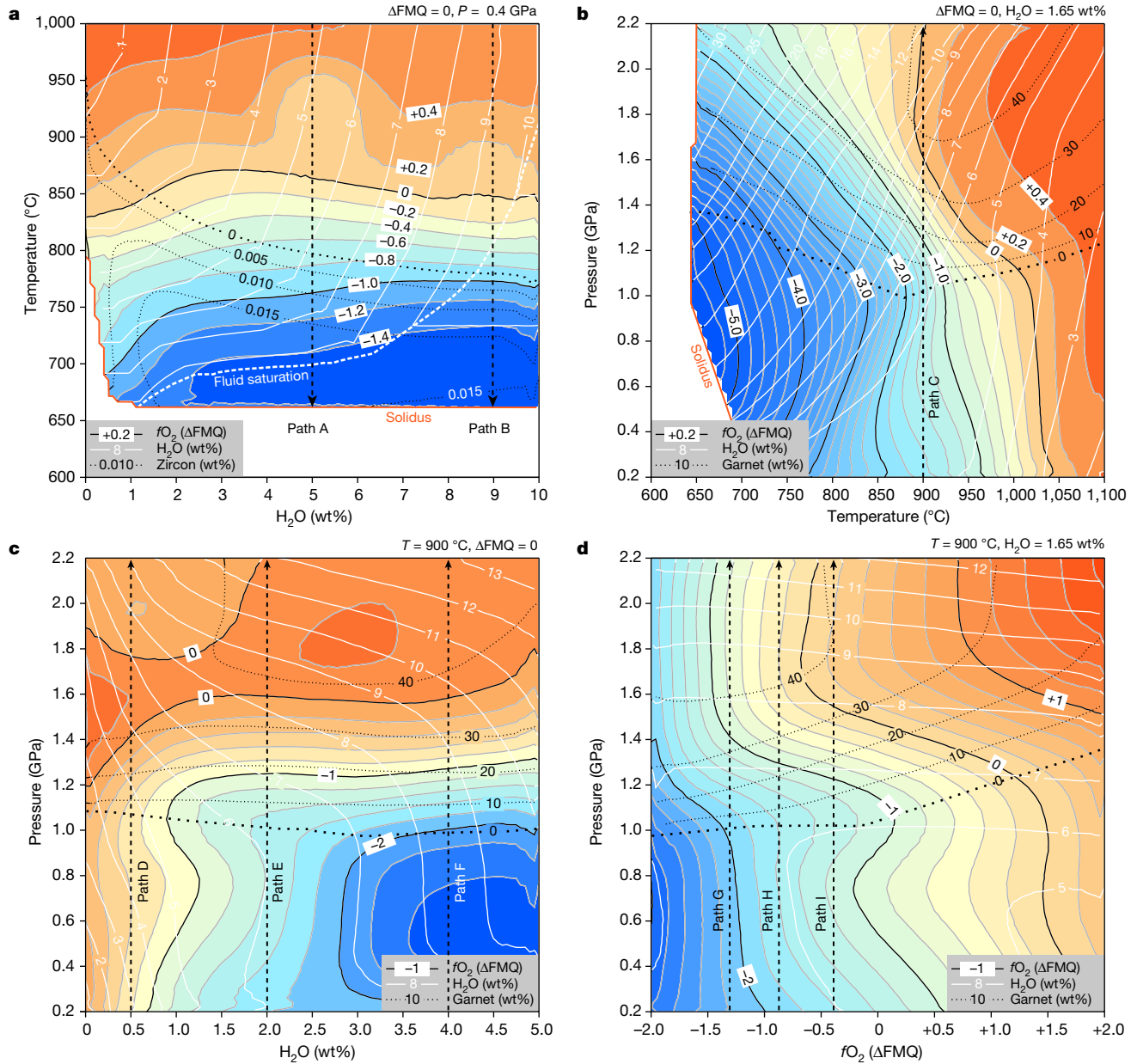


Fig. 3 | Thermodynamic-geochemical modelling of $f\text{O}_2$ and H_2O contents of TTG magmas. **a**, Crystallization of a median sodic TTG magma¹⁵ with different H_2O contents at 0.4 GPa, assuming initial $\Delta\text{FMQ} = 0$ at 800 °C. Paths A and B correspond to H_2O -undersaturated and H_2O -saturated crystallization of magmas with initial H_2O contents of 5 wt% and 9 wt%, respectively. Note the decrease of $f\text{O}_2$ with decreasing temperature and crystallization, so that the ΔFMQ values recorded in zircon probably underestimate the initial magmatic $f\text{O}_2$ by at least 0.6–0.8 log units. **b–d**, Differentiation of a median-enriched Archaean basalt³⁰, either by partial melting or fractional crystallization, to produce TTG magmas. **b**, Pressure–temperature (P – T) diagram, calculated at $\Delta\text{FMQ} = 0, \text{H}_2\text{O} = 1.65 \text{ wt\%}$.

with $\text{H}_2\text{O} = 1.65 \text{ wt\%}$ and $\Delta\text{FMQ} = 0$. The increase of pressure (path C) can explain the simultaneous increase of magmatic H_2O and $f\text{O}_2$ in TTG melts. **c**, P – H_2O diagram, calculated at $\Delta\text{FMQ} = 0$ and $T = 900 \text{ °C}$. **d**, P – $f\text{O}_2$ diagram, calculated at $\text{H}_2\text{O} = 1.65 \text{ wt\%}$ and $T = 900 \text{ °C}$. Note that differentiation of ambient mantle-derived magmas with low H_2O (≤ 0.5 , path D) and low magmatic $f\text{O}_2$ ($\Delta\text{FMQ} = -1.3$, path G)¹⁴ cannot explain the observed high magmatic H_2O (up to 10 wt%) and $f\text{O}_2$ ($\Delta\text{FMQ} \geq 0$) even at high pressures (such as 2.0 GPa), whereas modified mantle-derived magmas with elevated $f\text{O}_2$ and H_2O (ref. 14; paths E–I) readily explain these values. See Extended Data Fig. 5 for phase diagrams and Supplementary Table 4 for calculated melt compositions.

implication is that at least some hydration and oxidation (process 3) is needed to generate the mafic source of most Archaean TTGs.

An H_2O -rich magma source for Archaean granitoids is supported by their high $\text{H}_2\text{O}/\text{Ce}$ ratios (mostly $>1,000$; Supplementary Table 3). Because H_2O and Ce are similarly incompatible in most minerals, $\text{H}_2\text{O}/\text{Ce}$ ratios are not substantially affected by fractional crystallization or partial melting^{19,32}, except at fluid-saturated or near-solidus conditions (Extended Data Fig. 7). Our modelling shows that the high $\text{H}_2\text{O}/\text{Ce}$ ratios of groups 2 and 3 Archaean granitoids (medians of 1,252 and 2,338, respectively) reflect about 1.5–2 and 3–4 wt% H_2O in their magma

sources, respectively (Extended Data Fig. 7). The former is similar to the maximum H_2O content of mafic rocks that can be stored in hydrous minerals (Extended Data Fig. 8) and therefore can be explained by dehydration melting. The latter, however, requires excess H_2O and thus supports H_2O -fluxed melting of the mafic sources^{30,31,34}. Alternatively, the variably high $\text{H}_2\text{O}/\text{Ce}$ ratios may have been inherited from basaltic magmas (in the fractional crystallization scenario) resulting from H_2O -fluxed melting of the mantle^{8,9,32}. This is supported by the broadly positive correlation between $\text{H}_2\text{O}/\text{Ce}$ and Ba/La ratios of Archaean granitoids, similar to that observed in modern arc magmas³² (Extended

Data Fig. 9a). A positive correlation also exists between $\text{H}_2\text{O}/\text{Ce}$ and Sr/Y ratios (Extended Data Fig. 9b), suggesting a deep H_2O -rich source in the lower crust or the mantle.

Geodynamic implications

A deep, H_2O -rich magma source is a substantial challenge to the non-subduction models of Archaean TTG formation^{3–7}. The proposed H_2O sources in these models include: (1) primordial mantle-derived magmatic H_2O (ref. 6) and (2) hydrous minerals in altered mafic–ultramafic volcanic rocks (greenstones), which are transported down to the lower crust or even the mantle through greenstone ‘drips’^{5–7} or bulk burial by subsequent volcanic eruptions^{3,4}. However, the viability and efficiency of these mechanisms remain to be tested, because: (1) mantle-derived magmas unrelated to subduction are relatively dry^{8–10,18,19} and any H_2O (typically <0.5 wt%) would be concentrated in evolved magmas that migrate upwards, rather than stored in the lower crust³⁵; (2) greenstone ‘drips’ are driven by density contrast with the buoyant TTG domes^{5–7} and are unlikely to penetrate the lower crust or the mantle, which are also mafic–ultramafic and thus have similar density; and (3) even if they are transported to the melting depth, most H_2O would have been lost owing to prograde dehydration³⁵. More notably, the positive correlations of magmatic $f\text{O}_2$, H_2O contents and $\text{H}_2\text{O}/\text{Ce}$ ratios with depth of magma formation documented above (Fig. 2 and Extended Data Figs. 3 and 9b) are inconsistent with the top-down H_2O transport process predicted by these models. Instead, subduction of hydrated oceanic slabs provides an efficient way to deliver large amounts of oxidizing fluids into the mantle^{8–10,18,19}, and subsequent upward H_2O transport from the slab surface to arc lower crust readily explains the observed correlations. We conclude that, although the plume-related^{5,6} or impact-related⁷ models may be able to explain relatively dry, reducing and shallowly derived silicic magmas such as the 4.02-Ga high-Fe tonalite/diorite of the Acasta complex^{28,29}, large-scale, H_2O -rich and relatively oxidizing TTG magmas require substantial H_2O transport to the deep crust and mantle and were probably formed by subduction, through partial melting of subducting oceanic slabs^{1,31} and/or partial melting/fractionation at the base of arcs^{2,30}.

We also observe an overall increase in magmatic $f\text{O}_2$ and H_2O in granitoids during the Eoarchaean (4.0–3.6 Ga; Fig. 4a,b). This is supported by recent Ti (ref. 36) and Si (ref. 37) isotope studies that documented a transition from tholeiitic to calc-alkaline magmatism and onset of recycling of hydrated crust, respectively, during this period. This also coincides with a positive shift in initial zircon Hf isotope compositions³⁸ (Fig. 4c) and increases in whole-rock Sr/Y and La/Yb ratios²⁹. These observations are difficult to reconcile with a long-lived stagnant-lid geodynamic regime but can be explained by a notable transition from stagnant-lid to mobile-lid tectonics during the Eoarchaean, marked by the initiation of subduction and deep-water recycling. Notably, there is no marked difference in magmatic $f\text{O}_2$ and H_2O between early and late Archaean granitoids, challenging a popular view of subduction initiation some time between 3.2 and 2.5 Ga (refs. 3,5,7). This is further supported by geological records of many cratons, in which rock assemblages, geochemical characteristics and structural deformation akin to those in Phanerozoic accretionary orogens have been documented throughout the Archaean³⁹. Also, palaeomagnetic studies have documented large-scale horizontal motion in the Pilbara Craton at 3.34–3.18 Ga (ref. 40), whereas seismic profiles have revealed dipping reflections that extend into the mantle beneath the Superior and Yilgarn cratons⁴¹, supporting subduction throughout the Archaean.

Our data therefore reinforce the critical role of H_2O and plate tectonics in the formation of large-scale continental crust and evolution of habitable planets^{34,42}. Archaean plate tectonics, however, was probably different, characterized by episodic subduction of numerous smaller and thicker oceanic slabs, punctuated by frequent slab breakoff owing to a weaker lithosphere resulting from a hotter mantle^{39,43}. Such

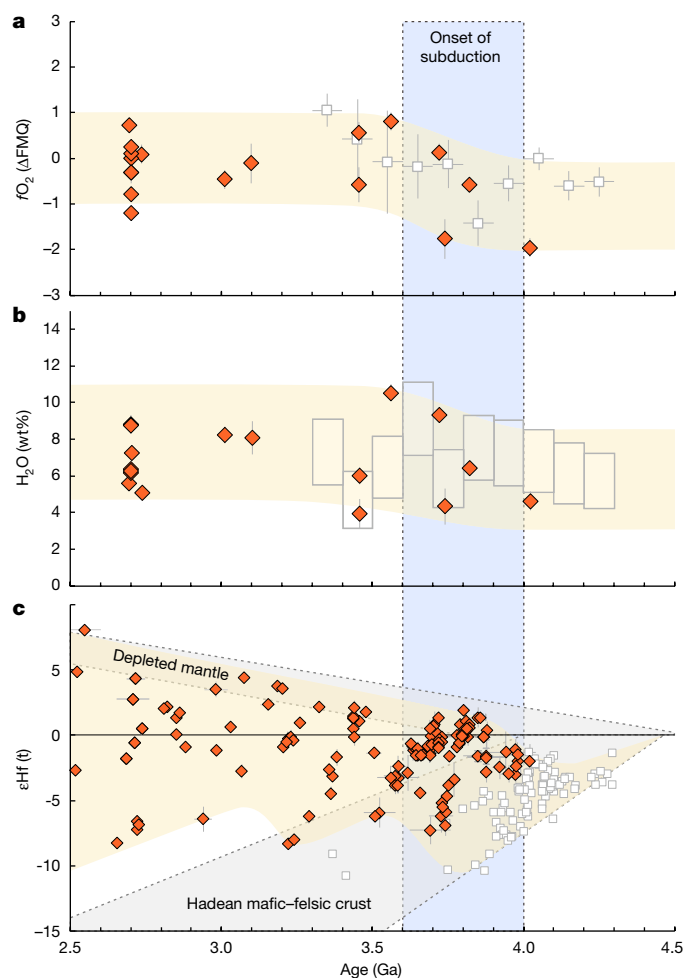


Fig. 4 | Increase of magmatic $f\text{O}_2$, H_2O content and zircon ϵHf suggests initiation of subduction during the Eoarchaean (4.0–3.6 Ga). **a**, Variation of magmatic $f\text{O}_2$ with age. **b**, Variation of magmatic H_2O content with age. **c**, Variation of magmatic zircon ϵHf isotope composition with age. Diamonds in **a** and **b** are data for Archaean granitoids (error bars are 2 s.e.m.). Squares in **a** are median ΔFMQ values for the Jack Hills zircons binned per 100 Myr, whereas rectangles in **b** show the ranges of model H_2O contents for the Jack Hills zircons calculated assuming a variety of source compositions, including the 4.02-Ga Acasta high-Fe tonalite/diorite²⁹, Archaean sodic TTG and potassio granitoids¹⁵, Archaean–Proterozoic strongly peraluminous granites⁴⁸ and residual granitic melts⁴⁷. Note the appearance of wet and oxidizing magmas and the elevation of the overall range of magmatic $f\text{O}_2$ and H_2O during 4.0–3.6 Ga, which largely remains constant afterwards, although data for magmatic rocks are still sparse for 3.5–2.8 Ga and there are large variations in the model H_2O contents of the Jack Hills zircons after 3.9 Ga. Zircon ϵHf values in **c** are weighted means for samples of Archaean granitoids with homogeneous Hf isotopic compositions (diamonds; error bars are 2σ), as compiled in refs. 30,31, whereas data for the Jack Hills zircons (squares) are individual concurrent Hf–Pb analyses⁴⁹.

subduction was probably less efficient in H_2O transport. Nonetheless, substantial amounts of surface H_2O could have been delivered to the lower crust and mantle^{18,19}. It is this process that would trigger large-scale TTG magmatism and rapid crustal growth in numerous proto-arcs^{30,31}. Subsequent arc accretion and enhanced crustal reworking would lead to large and stable continents, promoting evolution of plate tectonics to the style as we know it today³⁹.

Online content

Any methods, additional references, Nature Portfolio reporting summaries, source data, extended data, supplementary information,

acknowledgements, peer review information; details of author contributions and competing interests; and statements of data and code availability are available at <https://doi.org/10.1038/s41586-023-06552-0>.

1. Martin, H. Effect of steeper Archean geothermal gradient on geochemistry of subduction-zone magmas. *Geology* **14**, 753–756 (1986).
2. Rapp, R. P., Shimizu, N. & Norman, M. D. Growth of early continental crust by partial melting of eclogite. *Nature* **425**, 605–609 (2003).
3. Moore, W. B. & Webb, A. A. G. Heat-pipe Earth. *Nature* **501**, 501–505 (2013).
4. Rozel, A. B., Golabek, G. J., Jain, C., Tackley, P. J. & Gerya, T. Continental crust formation on early Earth controlled by intrusive magmatism. *Nature* **545**, 332–335 (2017).
5. Johnson, T. E., Brown, M., Gardiner, N. J., Kirkland, C. L. & Smithies, R. H. Earth's first stable continents did not form by subduction. *Nature* **543**, 239–242 (2017).
6. Smithies, R. H. et al. Oxygen isotopes trace the origins of Earth's earliest continental crust. *Nature* **592**, 70–75 (2021).
7. Johnson, T. E. et al. Giant impacts and the origin and evolution of continents. *Nature* **608**, 330–335 (2022).
8. Kelley, K. A. & Cottrell, E. Water and the oxidation state of subduction zone magmas. *Science* **325**, 605–607 (2009).
9. Zimmer, M. M. et al. The role of water in generating the calc-alkaline trend: new volatile data for Aleutian magmas and a new tholeiitic index. *J. Petrol.* **51**, 2411–2444 (2010).
10. Wallace, P. J., Plank, T., Edmonds, M. & Hauri, E. H. in *The Encyclopedia of Volcanoes* 2nd edn (eds Sigurdsson, H. et al.) 163–183 (Elsevier, 2015).
11. Smythe, D. J. & Brenan, J. M. Magmatic oxygen fugacity estimated using zircon-melt partitioning of cerium. *Earth Planet. Sci. Lett.* **453**, 260–266 (2016).
12. Loucks, R. R., Fiorentini, M. L. & Henriquez, G. J. New magmatic oxybarometer using trace elements in zircon. *J. Petrol.* **61**, egaa34 (2020).
13. Aulbach, S. & Stagni, V. Evidence for a reducing Archean ambient mantle and its effects on the carbon cycle. *Geology* **44**, 751–754 (2016).
14. Gao, L. et al. Oxidation of Archean upper mantle caused by crustal recycling. *Nat. Commun.* **13**, 3283 (2022).
15. Moyen, J. The composite Archean grey gneisses: petrological significance, and evidence for a non-unique tectonic setting for Archean crustal growth. *Lithos* **123**, 21–36 (2011).
16. Hoffmann, J. E., Zhang, C. & Nagel, T. in *Earth's Oldest Rocks* 2nd edn (eds Van Kranendonk, M. J. et al.) 133–168 (Elsevier, 2015).
17. Waters, L. E. & Lange, R. A. An updated calibration of the plagioclase-liquid hygrometer-thermometer applicable to basalts through rhyolites. *Am. Mineral.* **100**, 2172–2184 (2015).
18. Sobolev, A. V. et al. Komatiites reveal a hydrous Archean deep-mantle reservoir. *Nature* **531**, 628–632 (2016).
19. Sobolev, A. V. et al. Deep hydrous mantle reservoir provides evidence for crustal recycling before 3.3 billion years ago. *Nature* **571**, 555–559 (2019).
20. Smythe, D. J. & Brenan, J. M. Cerium oxidation state in silicate melts: combined FO_2 , temperature and compositional effects. *Geochim. Cosmochim. Acta* **170**, 173–187 (2015).
21. Meng, X. et al. Variable modes of formation for tonalite–trondhjemite–granodiorite–diorite (TTG)-related porphyry-type Cu ± Au deposits in the Neoarchean southern Abitibi subprovince (Canada): evidence from petrochronology and oxybarometry. *J. Petrol.* **62**, egab079 (2021).
22. Lu, Y. et al. *Zircon Fingerprinting of Magmatic-Hydrothermal Systems in the Archean Yilgarn Craton* (Geological Survey of Western Australia Report 197, 2019).
23. Lu, Y.-J. et al. in *Tectonics and Metallogeny of the Tethyan Orogenic Belt* Vol. 19 (ed. Richards, J. P.) 329–347 (Society of Economic Geologists, 2016).
24. Lu, Y., Loucks, R. R., Fiorentini, M. L., Yang, Z. & Hou, Z. Fluid flux melting generated postcollisional high Sr/Y copper ore-forming water-rich magmas in Tibet. *Geology* **43**, 583–586 (2015).
25. Bell, E. A., Boehnke, P. & Harrison, T. M. Recovering the primary geochemistry of Jack Hills zircons through quantitative estimates of chemical alteration. *Geochim. Cosmochim. Acta* **191**, 187–202 (2016).
26. Bouvier, A. et al. Li isotopes and trace elements as a petrogenetic tracer in zircon: insights from Archean TTGs and sanukitoids. *Contrib. Mineral. Petrol.* **163**, 745–768 (2012).
27. Laurent, O., Moyen, J., Wotzlaw, J., Björnsen, J. & Bachmann, O. Early Earth zircons formed in residual granitic melts produced by tonalite differentiation. *Geology* **50**, 437–441 (2021).
28. Reimink, J. R., Davies, J. H. F. L., Bauer, A. M. & Chacko, T. A. A comparison between zircons from the Acasta Gneiss Complex and the Jack Hills region. *Earth Planet. Sci. Lett.* **531**, 115975 (2020).
29. Reimink, J. R., Chacko, T., Stern, R. A. & Heaman, L. M. The birth of a cratonic nucleus: lithogeochemical evolution of the 4.02–2.94 Ga Acasta Gneiss Complex. *Precambrian Res.* **281**, 453–472 (2016).
30. Ge, R., Wilde, S. A., Zhu, W., Zhou, T. & Si, Y. Formation and evolution of Archean continental crust: a thermodynamic–geochemical perspective of granitoids from the Tarim Craton, NW China. *Earth-Sci. Rev.* **234**, 104219 (2022).
31. Ge, R., Zhu, W., Wilde, S. A. & Wu, H. Remnants of Eoarchean continental crust derived from a subducted proto-arc. *Sci. Adv.* **4**, aao3159 (2018).
32. Rasmussen, D. J., Plank, T. A., Roman, D. C. & Zimmer, M. M. Magmatic water content controls the pre-eruptive depth of arc magmas. *Science* **375**, 1169–1172 (2022).
33. Tang, M., Erdman, M., Eldridge, G. & Lee, C. A. The redox “filter” beneath magmatic orogens and the formation of continental crust. *Sci. Adv.* **4**, eaar4444 (2018).
34. Collins, W. J., Murphy, J. B., Johnson, T. E. & Huang, H. Critical role of water in the formation of continental crust. *Nat. Geosci.* **13**, 331–338 (2020).
35. Roman, A. & Arndt, N. Differentiated Archean oceanic crust: its thermal structure, mechanical stability and a test of the sagduction hypothesis. *Geochim. Cosmochim. Acta* **278**, 65–77 (2020).
36. Aarons, S. M. et al. Titanium isotopes constrain a magmatic transition at the Hadean–Archean boundary in the Acasta Gneiss Complex. *Sci. Adv.* **6**, eabc9959 (2020).
37. Zhang, Q. et al. No evidence of supracrustal recycling in Si–O isotopes of Earth's oldest rocks 4 Ga ago. *Sci. Adv.* **9**, eadf693 (2023).
38. Bauer, A. M. et al. Hafnium isotopes in zircons document the gradual onset of mobile-lid tectonics. *Geochim. Perspect. Lett.* **14**, 1–6 (2020).
39. Windley, B. F., Kusky, T. & Polat, A. Onset of plate tectonics by the Eoarchean. *Precambrian Res.* **352**, 105980 (2021).
40. Brenner, A. R., Fu, R. R., Kylander-Clark, A. R., Hudak, G. J. & Foley, B. J. Plate motion and a dipolar geomagnetic field at 3.25 Ga. *Proc. Natl Acad. Sci. USA* **119**, e2084709177 (2022).
41. Calvert, A. J., Doublier, M. P. & Sellars, S. E. Seismic reflections from a lithospheric suture zone below the Archean Yilgarn Craton. *Nat. Commun.* **12**, 7245 (2021).
42. Campbell, I. H. & Taylor, S. R. No water, no granites - no oceans, no continents. *Geophys. Res. Lett.* **10**, 1061–1064 (1983).
43. van Hunen, J. & Moyen, J. Archean subduction: fact or fiction? *Annu. Rev. Earth Planet. Sci.* **40**, 195–219 (2012).
44. Wallace, P. J., Anderson, A. T. Jr & Davis, A. M. Gradients in H_2O , CO_2 , and exsolved gas in a large-volume silicic magma system: interpreting the record preserved in melt inclusions from the Bishop Tuff. *J. Geophys. Res. Solid Earth* **104**, 20097–20122 (1999).
45. Gudelius, D. et al. Zircon melt inclusions in mafic and felsic rocks of the Bushveld Complex—constraints for zircon crystallization temperatures and partition coefficients. *Geochim. Cosmochim. Acta* **289**, 158–181 (2020).
46. Watts, K. E. & Mercer, C. N. Zircon-hosted melt inclusion record of silicic magmatism in the Mesoproterozoic St. Francois Mountains terrane, Missouri: origin of the Pea Ridge iron oxide-apatite-rare earth element deposit and implications for regional crustal pathways of mineralization. *Geochim. Cosmochim. Acta* **272**, 54–77 (2020).
47. Laurent, O. et al. Earth's earliest granitoids are crystal-rich magma reservoirs tapped by silicic eruptions. *Nat. Geosci.* **13**, 163–169 (2020).
48. Bucholz, C. E., Stolper, E. M., Eiler, J. M. & Breaks, F. W. A comparison of oxygen fugacities of strongly peraluminous granites across the Archean–Proterozoic boundary. *J. Petrol.* **59**, 2123–2156 (2018).
49. Kemp, A. I. S. et al. Hadean crustal evolution revisited: new constraints from Pb–Hf isotope systematics of the Jack Hills zircons. *Earth Planet. Sci. Lett.* **296**, 45–56 (2010).

Publisher's note Springer Nature remains neutral with regard to jurisdictional claims in published maps and institutional affiliations.

Springer Nature or its licensor (e.g. a society or other partner) holds exclusive rights to this article under a publishing agreement with the author(s) or other rightsholder(s); author self-archiving of the accepted manuscript version of this article is solely governed by the terms of such publishing agreement and applicable law.

© The Author(s), under exclusive licence to Springer Nature Limited 2023

Methods

The zircon oxybarometer-hygrometer

On the basis of experimental work²⁰, Smythe and Brenan¹¹ established an oxybarometer to estimate the $f\text{O}_2$ of magma in equilibrium with zircon:

$$\ln \left[\frac{x_{\text{Ce}^{4+}}^{\text{melt}}}{x_{\text{Ce}^{3+}}^{\text{melt}}} \right] = \frac{1}{4} \ln f\text{O}_2 + \frac{13,136(\pm 591)}{T} - 2.064(\pm 0.011) \frac{\text{NBO}}{T} - 8.878(\pm 0.112) \times x\text{H}_2\text{O} - 8.955(\pm 0.091) \quad (1)$$

in which $\frac{x_{\text{Ce}^{4+}}^{\text{melt}}}{x_{\text{Ce}^{3+}}^{\text{melt}}}$ is the $\text{Ce}^{4+}/\text{Ce}^{3+}$ ratio of melt estimated using the lattice strain model⁵⁰ based on zircon–melt partitioning of trivalent (Y and rare-earth elements) and tetravalent (Zr, Hf, Ti, Th and U) cations; T is temperature in degrees kelvin calculated using the Ti-in-zircon thermometer⁵¹; NBO/T is the proportion of non-bridging oxygens to tetrahedrally coordinated cations; and $x\text{H}_2\text{O}$ is the molar fraction of H_2O dissolved in the melt. According to equation (1), magmatic $f\text{O}_2$ and H_2O content are positively correlated for a given zircon–melt pair (Fig. 1a), so that magmatic H_2O content can be determined if $f\text{O}_2$ can be estimated independently.

On the basis of thermodynamic considerations and empirical calibration, Loucks et al.¹² proposed an independent oxybarometer based on Ce, U and Ti contents (ppm) in zircon:

$$\Delta\text{FMQ} = 3.998(\pm 0.124) \log(\text{Ce}/\sqrt{\text{U}_i \times \text{Ti}}) + 0.2284(\pm 0.101) \quad (2)$$

in which ΔFMQ is magmatic $f\text{O}_2$ relative to the FMQ buffer and U_i is initial U corrected for radioactive decay. Accordingly, the magmatic $f\text{O}_2$ values obtained using equation (2) can be used as an input to equation (1) to retrieve equilibrium magmatic H_2O content (that is, a zircon oxybarometer-hygrometer; Supplementary Information).

This is illustrated in Fig. 1a using the zircon and melt (inclusions in quartz) compositions of the Ig2E unit of the Bishop Tuff (California)¹¹, for which the Ce-U-Ti oxybarometer yields a median ΔFMQ value of $+1.22 \pm 0.28$ (2 s.e.m.), corresponding to a magmatic H_2O content of 5.8 ± 0.6 wt% (2 s.e.m.), in good agreement with the H_2O content determined independently from melt inclusions (5.7 ± 0.6 wt%, 2 s.d.)⁴⁴.

To further test the applicability and accuracy of the zircon oxybarometer-hygrometer, modern to Archaean zircon–melt/whole-rock pairs with well-constrained magmatic H_2O contents were selected from different tectonic settings (inset in Fig. 1a and Supplementary Tables 1–3). Melt inclusions in zircon provide the best estimate of the equilibrium melt composition when the mineral crystallized. Zircon-hosted melt inclusions from the 2.055-Ga Bushveld Complex (South Africa)⁴⁵ and the 1.46-Ga Pea Ridge rhyolitic tuff (sample PR-12, USA)⁴⁶ have median H_2O contents of 2.4 ± 1.2 and 2.5 ± 0.8 wt% (2 s.d., excluding data from fractured melt inclusions), respectively, according to ion microprobe analyses. Using the median zircon and melt inclusion compositions^{45,46}, the zircon oxybarometer-hygrometer yields H_2O contents of 1.8 ± 0.6 and 3.4 ± 1.1 wt% (2 s.e.m.) for the Bushveld Complex and Pea Ridge rhyolite, respectively, illustrating the low magmatic H_2O contents of evolved melts from anorogenic or intracratonic settings.

Like the Bishop Tuff, the Toba Tuff (Indonesia) is typical of felsic magmas with higher H_2O contents that are formed above active subduction zones. Using the median zircon composition of the Younger Toba Tuff¹¹, the zircon oxybarometer-hygrometer yields an H_2O content of 6.9 ± 0.5 wt% (2 s.e.m.), which is higher than the H_2O contents of quartz-hosted melt inclusions (4.7 ± 1.4 wt%, 2 s.d.)⁵², but is consistent with the results of the plagioclase hygrometer (6.6 – 7.9 wt%)¹⁷. This can be accounted for by experimental results showing that plagioclase crystallized at higher pressures in less degassed magmas than quartz¹⁷. It is likely that zircon crystallized along with plagioclase, as indicated by the negative correlation between the Eu anomaly and Hf content

in zircon (Extended Data Fig. 4). This indicates the potential of the zircon oxybarometer-hygrometer for retrieving H_2O contents of less degassed magmas, as would be applicable in relatively deep crustal magma reservoirs.

Archaean igneous rocks with known magmatic H_2O contents are rare. Laurent et al.⁴⁷ reported quartz-hosted melt inclusions in the well-preserved Palaeoarchaean (3.46-Ga) felsic meta-volcanic rocks from the Barberton Greenstone Belt (South Africa). The H_2O contents were not measured, but the maximum values can be estimated to be 4.8–6.4 wt% (median 5.5 ± 1.2 wt%, 2 s.d.) based on the difference in the total of major oxides from 100 wt%. Using the median zircon compositions reported in ref. 27, the zircon oxybarometer-hygrometer yields an H_2O content of 6.3 ± 0.8 wt% (2 s.e.m.), demonstrating its applicability to Archaean magmas. We conclude that the zircon oxybarometer-hygrometer is able to retrieve the median magmatic H_2O content during zircon crystallization within about 1 wt% uncertainty (inset in Fig. 1a).

The uncertainty of the zircon oxybarometer-hygrometer derives from: (1) analytical uncertainties in zircon and melt/whole-rock compositions; (2) calibration uncertainties of both oxybarometers; and (3) zircon–melt disequilibrium. The analytical uncertainties are typically $\leq 5\%$ for major elements and $\leq 10\%$ for trace elements, producing an uncertainty of ≤ 0.13 and ≤ 0.17 log units for the $\text{Ce}^{4+}/\text{Ce}^{3+}$ and Ce-U-Ti oxybarometers, respectively, which propagate to an uncertainty of ≤ 0.6 wt% in magmatic H_2O content. The calibration uncertainties of the $\text{Ce}^{4+}/\text{Ce}^{3+}$ and Ce-U-Ti oxybarometers are approximately 1.0 and 0.6 log units, respectively^{11,12}, translating to an uncertainty in magmatic H_2O content of about 2.8 wt%. Accordingly, the total uncertainty of the zircon oxybarometer-hygrometer is estimated to be approximately 2.9 wt% (quadratic addition of analytical and calibration uncertainties). Consequently, H_2O contents obtained from single zircon/whole-rock analyses should be treated with caution.

The issue of zircon–melt disequilibrium is raised because zircon crystallizes from a continually evolving magma during gradual cooling. We use the median compositions of a group of spatial-temporally related zircons and melts/rocks to minimize the effect of this issue, and the obtained magmatic H_2O contents are considered as the median values during the zircon crystallization process. We further evaluated the effect of zircon crystallization in residual melt by calculating the H_2O content of the Barberton meta-rhyolite assuming zircon crystallizing in a residual melt that is represented by quartz-hosted melt inclusions^{27,47} (Extended Data Fig. 2a). This yields an apparent magmatic H_2O content of 4.9 ± 0.8 wt% (2 s.e.m.), slightly lower, but within error, of that estimated from melt inclusion data (maximum 5.5 ± 1.2 wt%, 2 s.d.)⁴⁷ and by assuming zircon–whole-rock equilibrium (6.4 ± 0.8 wt%, 2 s.e.m.). However, thermodynamic modelling shows that most zircons crystallized earlier than quartz (see Fig. 3a in ref. 27) and therefore are in equilibrium with less evolved melts than those trapped as melt inclusions in quartz. Such slightly evolved melts have little effect on the estimate of magmatic H_2O content using the zircon oxybarometer-hygrometer.

Another potential issue with the assumption of zircon–whole-rock equilibrium is metamorphic disturbance of the whole-rock geochemical composition. Simple modelling (see Extended Data Fig. 2b) shows that preferential U loss, as indicated by high Th/U ratios (7.1–38.2) of several TTG suites (for example, the approximately 3.72-Ga Aktash gneisses), may lead to overestimates of magmatic H_2O content. We have corrected for this effect for these high-Th/UTTG suites by assuming $\text{Th}/\text{U} = 5$, according to the median composition of the global sodic TTGs¹⁵, which results in 0.5–2.4 wt% lower H_2O . The U loss-corrected H_2O contents, however, should be considered as minimum estimates because U loss may be accompanied by loss of light rare-earth elements (LREE) in extreme cases, which may partly compensate the effect of U loss (Extended Data Fig. 2b). Other elements involved in the calculations (for example, Zr, Hf, Ti, Th and major elements) are generally

resistant to metamorphism³⁰ or have little effect on H₂O content estimates (Extended Data Figs. 2b and 10).

Zircon trace-element analysis

New zircon trace-element data were obtained for well-preserved magmatic grains with clear oscillatory zoning from TTG gneisses of the approximately 3.7-Ga Aktash complex^{31,53} and the 3.2–3.0-Ga Heluositian complex³⁰ of the Tarim Craton, northwestern China. We carried out this analysis using a New Wave 193-nm laser ablation system with an in-house sample cell coupled to a Thermal iCAP RQ ICP-MS at the State Key Laboratory for Mineral Deposits Research, Nanjing University. All the analyses were conducted using a beam diameter of 30 μm, a repetition rate of 5 Hz and an energy of 10–20 J cm⁻². Mass fractionation was calibrated against standard glass NIST SRM 610 as the external standard in conjunction with internal standardization using ²⁹Si (15.32 wt% Si in zircon). Standard zircon GJ-1 was analysed along with unknowns to monitor the accuracy. Raw data were processed using the online software package GLITTER (version 4.4) (<http://www.glitter-gemoc.com/>).

Data compilation and filtering

Zircon and whole-rock elemental data were also compiled for Archaean granitoids worldwide (Extended Data Fig. 1 and Supplementary Tables 1–3), including the 4.02–3.56-Ga Acasta complex (Canada)^{28,29}, the 3.82-Ga Itsaq complex (Greenland)⁵⁴, the 3.46-Ga rocks from the Barberton area (South Africa)^{27,47} and the Neoproterozoic TTGs from the Superior⁵⁵, Yilgarn²³ and Tarim⁵⁶ cratons. Data for rare Archaean^{21,22} and typical Mesozoic–Cenozoic^{23,24} granitoids associated with PCDs, as well as detrital Hadean zircons from the Jack Hills (Australia)^{25,26}, were also compiled for comparison. Rock suites with only a small number (<5) of zircon analyses or a single whole-rock analysis were not included, considering the higher uncertainty (see above). For the whole-rock and zircon database of the Superior Craton⁵⁵, only data for TTGs were selected, based on whole-rock geochemical data (SiO₂ ≥ 63 wt% and K₂O/Na₂O ≤ 0.6) or lithological information (TTG). Some rare-earth element data, when not reported in the literature, are interpolated from adjacent elements, except for Eu and Ce. All the zircon data were filtered using the following criteria to extract the primary magmatic composition: (1) LREE-I ≥ 30 (ref. 25); (2) La ≤ 0.5 ppm; (3) Ca ≤ 150 ppm and Fe ≤ 150 ppm (if available); and (4) discordance of U-Pb ages (if available) within 5% and common Pb < 1%. The rationale for this filtering is discussed in refs. 25,27. The median values of the filtered zircon and whole-rock compositions, as well as the median ΔFMQ given by the zircon Ce-U-Ti oxybarometer, were used to calculate the equilibrium magmatic H₂O content using an Excel spreadsheet (Supplementary Information).

Thermodynamic–geochemical modelling

Thermodynamic modelling was carried out with the software GeoPS⁵⁷, using the thermodynamic database HP633 (ref. 58) and solution models for melt, fluid, garnet, clinopyroxene, orthopyroxene, olivine and spinel from ref. 59, amphibole from ref. 60, feldspar from ref. 61, muscovite, biotite and ilmenite from ref. 62 and epidote from ref. 58. Pseudosections were calculated for a median sodic TTG¹⁵ and a median-enriched Archaean basalt³⁰ in the P–T, T–H₂O, P–H₂O and P–fO₂ spaces. Mode (wt%) and major-element compositions of melts and equilibrium mineral assemblages were extracted at regular grids (40 × 40). The fO₂ of melts was calculated from major-element compositions (Fe₂O₃ contents were converted from O₂) using the relation given in ref. 63. Trace-element compositions of melts were calculated using the batch melting/crystallization equation:

$$C/C_0 = 1/[D + F(1 - D)] \quad (3)$$

in which C and C₀ are the concentrations of an element in the melt and source, respectively; F is the fraction of melt (in wt%); and D is the bulk

partitioning coefficient calculated using mineral mode and partitioning coefficient from ref. 64. The mode of zircon crystallized during cooling of TTG melts was calculated as follows:

$$X(\text{zircon}) = [\text{Zr}(\text{melt}) - \text{Zr}(\text{saturation})]/\text{Zr}(\text{zircon}) \times X(\text{melt}) \quad (4)$$

in which Zr(melt) is the Zr content (ppm) of melt calculated using equation (3); Zr(saturation) is the Zr content that saturates the melt according to the zircon saturation model of ref. 65; Zr(zircon) is the ideal Zr concentration in zircon (49.77 wt%); and X(melt) is the proportion of melt (in wt%). These modelling results are presented in Supplementary Table 4.

Data availability

New and compiled zircon trace-elemental data are presented in Supplementary Table 1. Compiled whole-rock elemental data are presented in Supplementary Table 2. Calculated median zircon and whole-rock/melt compositions, as well as the calculated magmatic fO₂ values and H₂O contents, are presented, along with their estimated uncertainties, in Supplementary Table 3. The results of thermodynamic–geochemical modelling are presented in Supplementary Table 4. All the supplementary data and the Excel spreadsheet used to calculate magmatic H₂O contents are available to download from the EarthChem library (<https://doi.org/10.26022/IEDA/112745>). Source data are provided with this paper.

50. Blundy, J. & Wood, B. Prediction of crystal–melt partition coefficients from elastic moduli. *Nature* **372**, 452–454 (1994).
51. Ferry, J. & Watson, E. New thermodynamic models and revised calibrations for the Ti-in-zircon and Zr-in-rutile thermometers. *Contrib. Mineral. Petrol.* **154**, 429–437 (2007).
52. Chesner, C. A. & Luhr, J. F. A melt inclusion study of the Toba Tuffs, Sumatra, Indonesia. *J. Volcanol. Geotherm. Res.* **197**, 259–278 (2010).
53. Ge, R. et al. Generation of Archaean continental crust from altered mafic rocks derived from a chondritic mantle: the ~3.72 Ga Aktash gneisses, Tarim Craton (NW China). *Earth Planet. Sci. Lett.* **538**, 116225 (2020).
54. Kielman, R., Whitehouse, M., Nemchin, A. & Kemp, A. A tonalitic analogue to ancient detrital zircon. *Chem. Geol.* **499**, 43–57 (2018).
55. Mole, D. R. et al. The formation of Neoproterozoic continental crust in the south-east Superior Craton by two distinct geodynamic processes. *Precambrian Res.* **356**, 106104 (2021).
56. Zong, K. Q. et al. The generation and evolution of Archean continental crust in the Dunhuang block, northeastern Tarim Craton, northwestern China. *Precambrian Res.* **235**, 251–263 (2013).
57. Xiang, H. & Connolly, J. A. D. GeoPS: an interactive visual computing tool for thermodynamic modelling of phase equilibria. *J. Metamorph. Geol.* **40**, 243–255 (2022).
58. Holland, T. J. B. & Powell, R. An improved and extended internally consistent thermodynamic dataset for phases of petrological interest, involving a new equation of state for solids. *J. Metamorph. Geol.* **29**, 333–383 (2011).
59. Holland, T. J. B., Green, E. C. R. & Powell, R. Melting of peridotites through to granites: a simple thermodynamic model in the system KNCFMASHTOCr. *J. Petrol.* **59**, 881–900 (2018).
60. Green, E. et al. Activity–composition relations for the calculation of partial melting equilibria in metabasic rocks. *J. Metamorph. Geol.* **34**, 845–869 (2016).
61. Holland, T. J. B., Green, E. C. R. & Powell, R. A thermodynamic model for feldspars in KAlSi₃O₈–NaAlSi₂O₈–CaAl₂Si₂O₈ for mineral equilibrium calculations. *J. Metamorph. Geol.* **40**, 587–600 (2022).
62. White, R. W., Powell, R. & Johnson, T. E. The effect of Mn on mineral stability in metapelites revisited: new a-x relations for manganese-bearing minerals. *J. Metamorph. Geol.* **32**, 809–828 (2014).
63. Kress, V. C. & Carmichael, I. S. The compressibility of silicate liquids containing Fe₂O₃ and the effect of composition, temperature, oxygen fugacity and pressure on their redox states. *Contrib. Mineral. Petrol.* **108**, 82–92 (1991).
64. Bédard, J. H. A catalytic delamination-driven model for coupled genesis of Archaean crust and sub-continental lithospheric mantle. *Geochim. Cosmochim. Acta* **70**, 1188–1214 (2006).
65. Watson, E. B. & Harrison, T. M. Zircon saturation revisited: temperature and composition effects in a variety of crustal magma types. *Earth Planet. Sci. Lett.* **64**, 295–304 (1983).
66. Furnes, H., Dilek, Y. & De Wit, M. Precambrian greenstone sequences represent different ophiolite types. *Gondwana Res.* **27**, 649–685 (2015).
67. Bea, F. & Montero, P. Behavior of accessory phases and redistribution of Zr, REE, Y, Th, and U during metamorphism and partial melting of metapelites in the lower crust: an example from the Kinzigite Formation of Ivrea-Verbano, NW Italy. *Geochim. Cosmochim. Acta* **63**, 1133–1153 (1999).

Article

Acknowledgements This work was supported by grants from the National Natural Science Foundation of China (41872191, 41922017 and 42025202).

Author contributions R.-F.G. conceived the project, collected the data, performed the modelling and wrote the original draft. S.A.W., W.-B.Z. and X.-L.W. contributed to analysis of the data and revision of the original draft.

Competing interests The authors declare no competing interests.

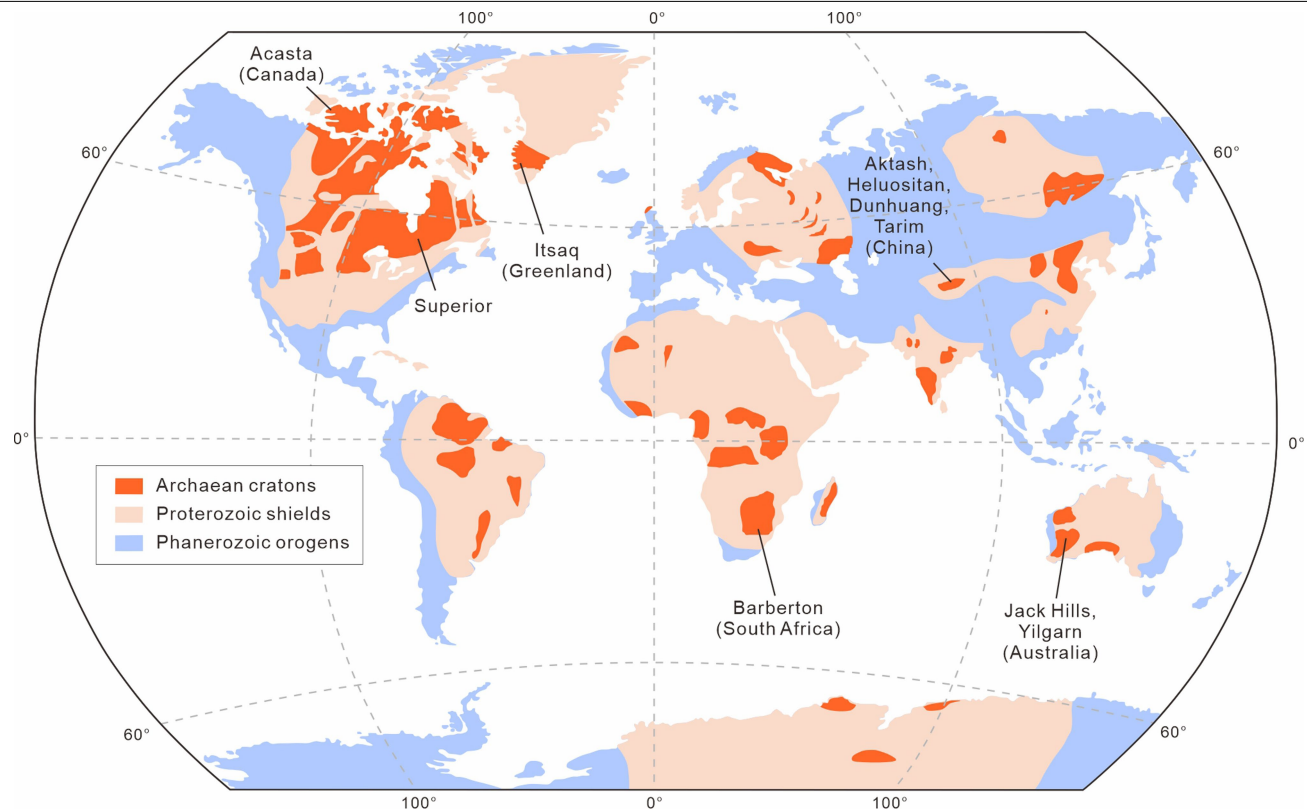
Additional information

Supplementary information The online version contains supplementary material available at <https://doi.org/10.1038/s41586-023-06552-0>.

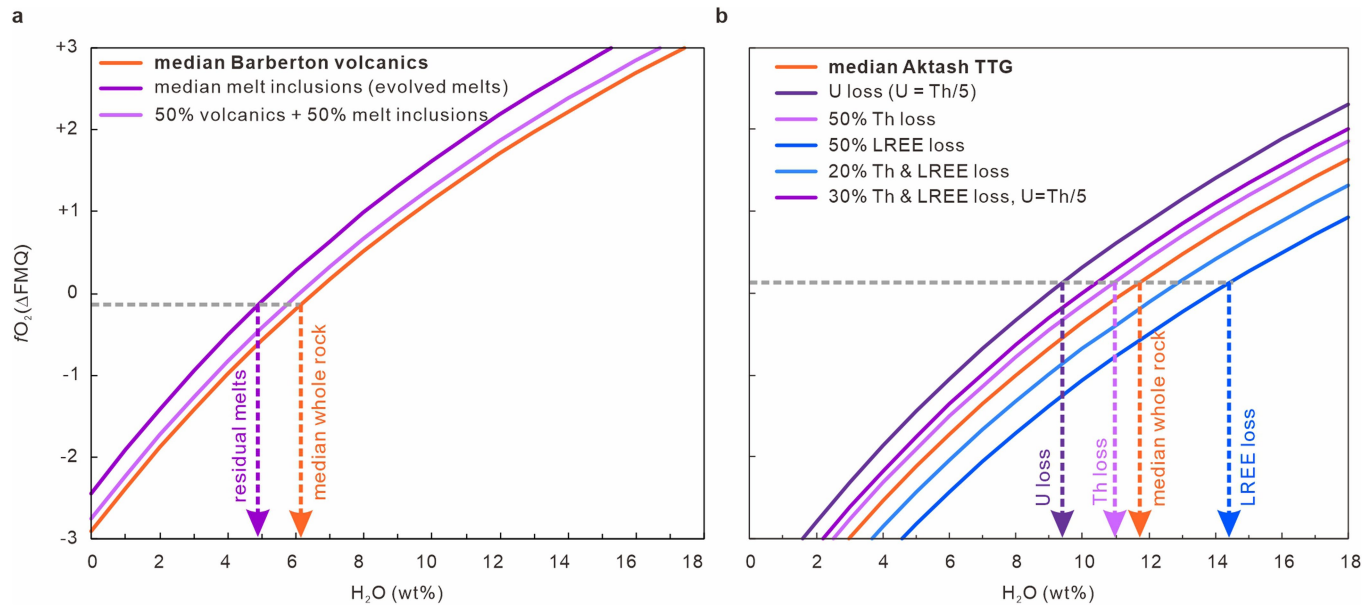
Correspondence and requests for materials should be addressed to Rong-Feng Ge.

Peer review information *Nature* thanks Elizabeth Bell and Marco Fiorentini for their contribution to the peer review of this work. Peer reviewer reports are available.

Reprints and permissions information is available at <http://www.nature.com/reprints>.

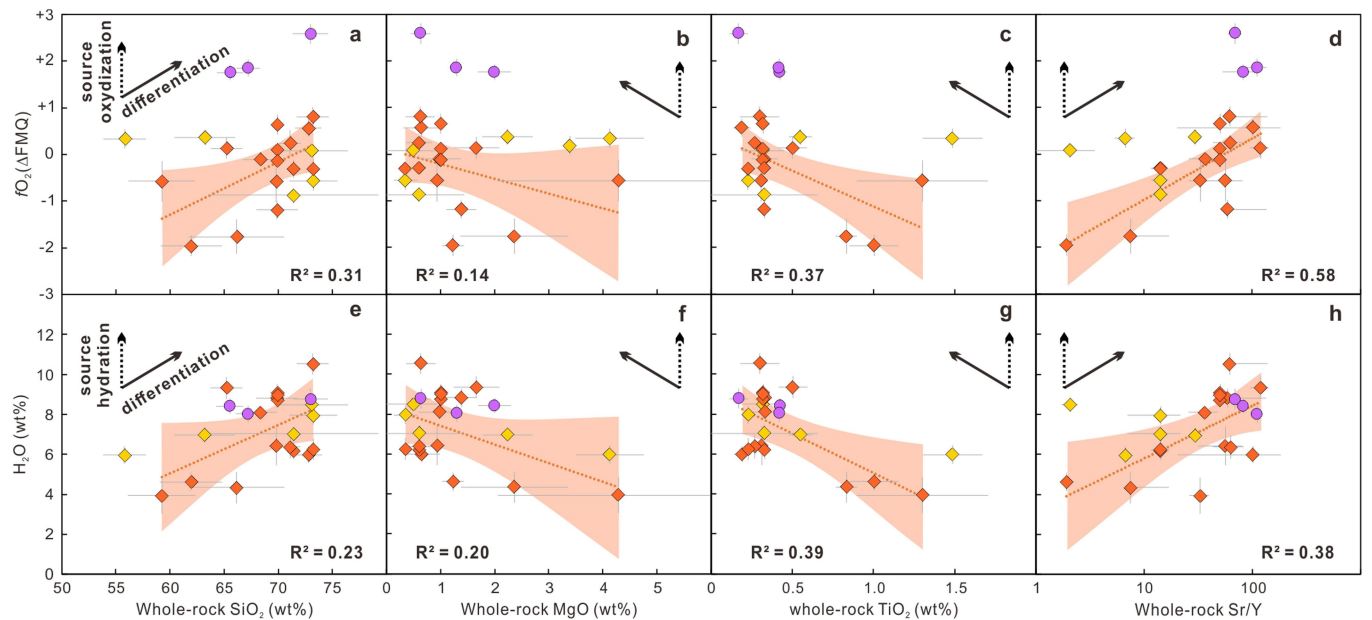


Extended Data Fig. 1 | Distribution of the rocks and zircons discussed in this study. Modified after ref. 66.

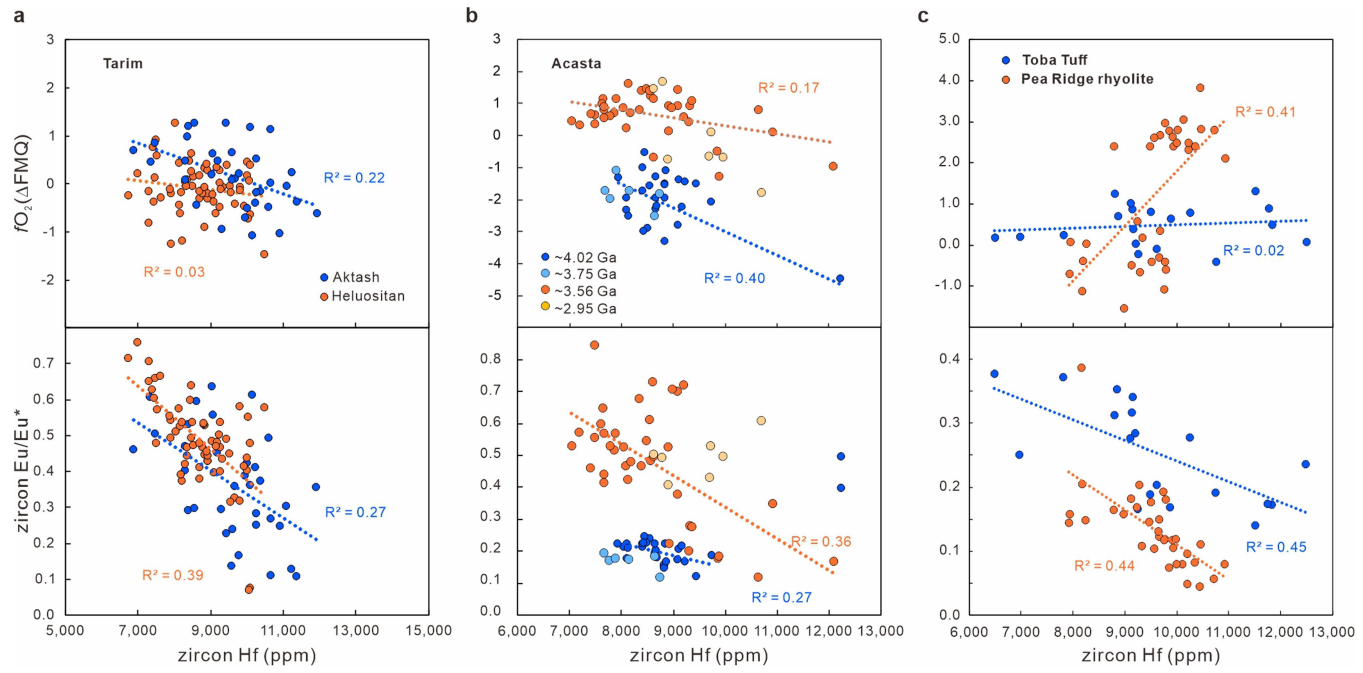


Extended Data Fig. 2 | The effect of zircon–whole-rock disequilibrium on magmatic H_2O estimate. **a**, The effect of zircon crystallization in evolved, residual melts after fractional crystallization, illustrated using data from the Palaeoarchaean (3.46-Ga) Barberton volcanic rocks^{27,47}. The orange curve shows the relationship based on median whole-rock and zircon compositions according to the zircon $\text{Ce}^{4+}/\text{Ce}^{3+}$ oxybarometer¹¹, whereas the dark purple curve is calculated using the median composition of quartz-hosted melt inclusions that represent residual melts^{27,47}. For a given ΔFMQ value (median -0.13 for the Barberton volcanic zircons), this results in approximately 1.5 wt% lower H_2O content (compare the orange and dark purple arrows). However, as most zircons crystallized earlier than quartz, according to thermodynamic-geochemical modelling²⁷, the slightly evolved melts (for example, the light purple curve) only have limited effect on the estimate of magmatic H_2O content (within 1 wt%). **b**, The effect of metamorphic disturbance of whole-rock composition, illustrated using data from the Eoarchaean (3.72-Ga) Aktash gneisses, Tarim Craton^{31,53}. Similarly, the orange curve shows the relationship between magmatic H_2O content and ΔFMQ for the median zircon (this study) and whole-rock compositions (Supplementary Table 3), whereas the other coloured curves show the effects of various metamorphic modifications of the

whole-rock composition, assuming other elements being constant. The vertical dashed lines with arrows show the corresponding changes in estimated magmatic H_2O content for a given ΔFMQ value (median 0.14 for the Aktash gneisses). This simple modelling shows that loss of U and Th during high-grade metamorphism or anatexis may result in overestimates of H_2O content, whereas loss of LREE has an opposite effect. Preferential U loss is indicated by the high Th/U ratios (7.1–38.2) of several Archaean TTG suites (for example, the 3.72-Ga Aktash complex^{31,53}), probably because of high-grade metamorphism and anatexis⁶⁷. By contrast, the Th and LREE contents of Archaean TTGs seem to be conservative, probably because of retention of these elements in monazite⁶⁷. Moreover, the opposite effect of Th-U and LREE loss means that, even if these elements were mobilized (for example, by partial dissolution of monazite in metamorphic fluids or anatexitic melts), their effects tend to compensate each other. Accordingly, we only corrected for the effect of U loss for TTG suites with high Th/U ratios (>7), by assuming a Th/U ratio of 5, the median value of the global sodic TTGs¹⁵, and the results are considered as minimum estimates of equilibrium magmatic H_2O content during zircon crystallization.

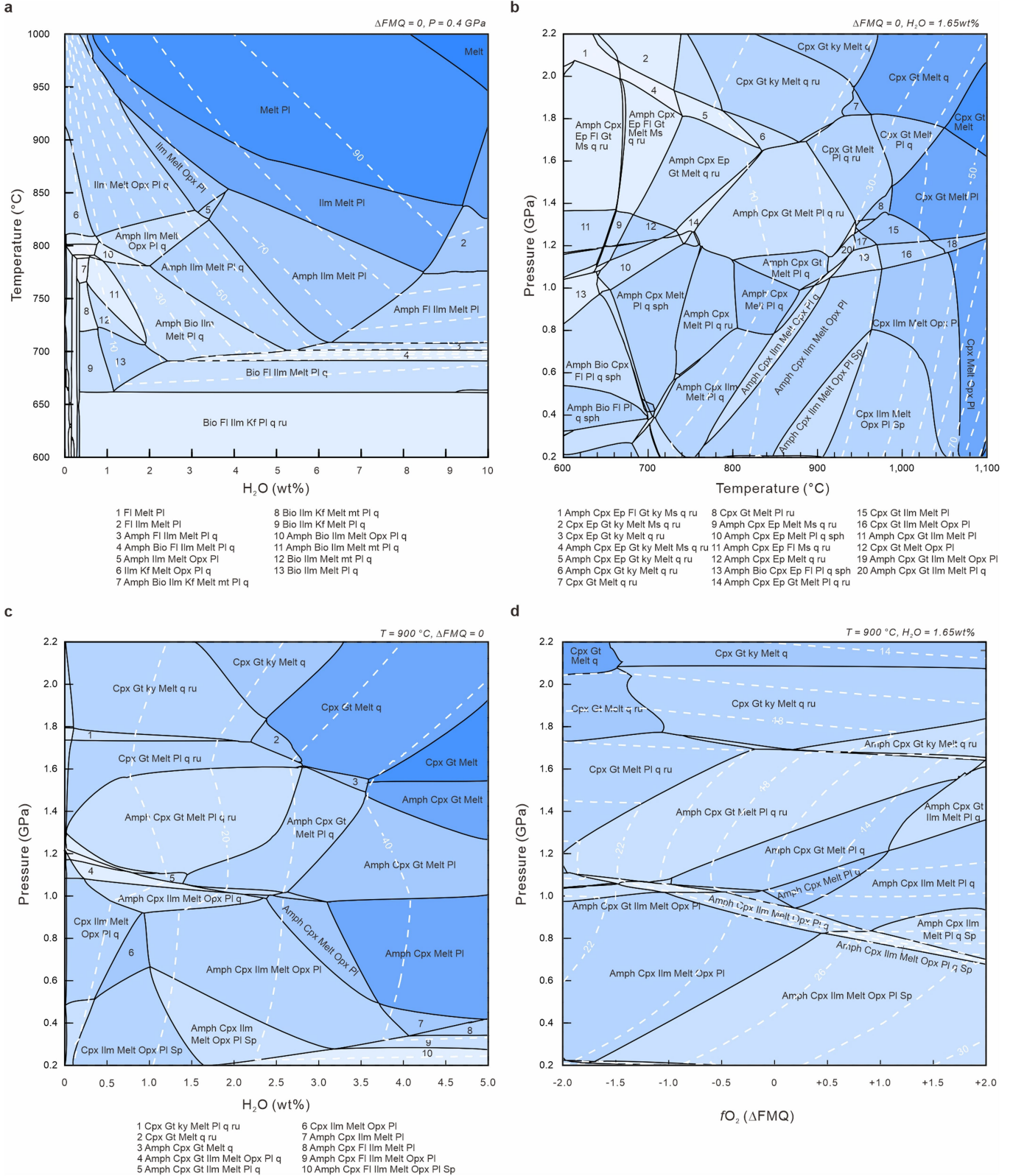


Extended Data Fig. 3 | Further diagrams showing correlations between whole-rock compositions and magmatic $f\text{O}_2$ and H_2O contents. See Fig. 2 for explanation.



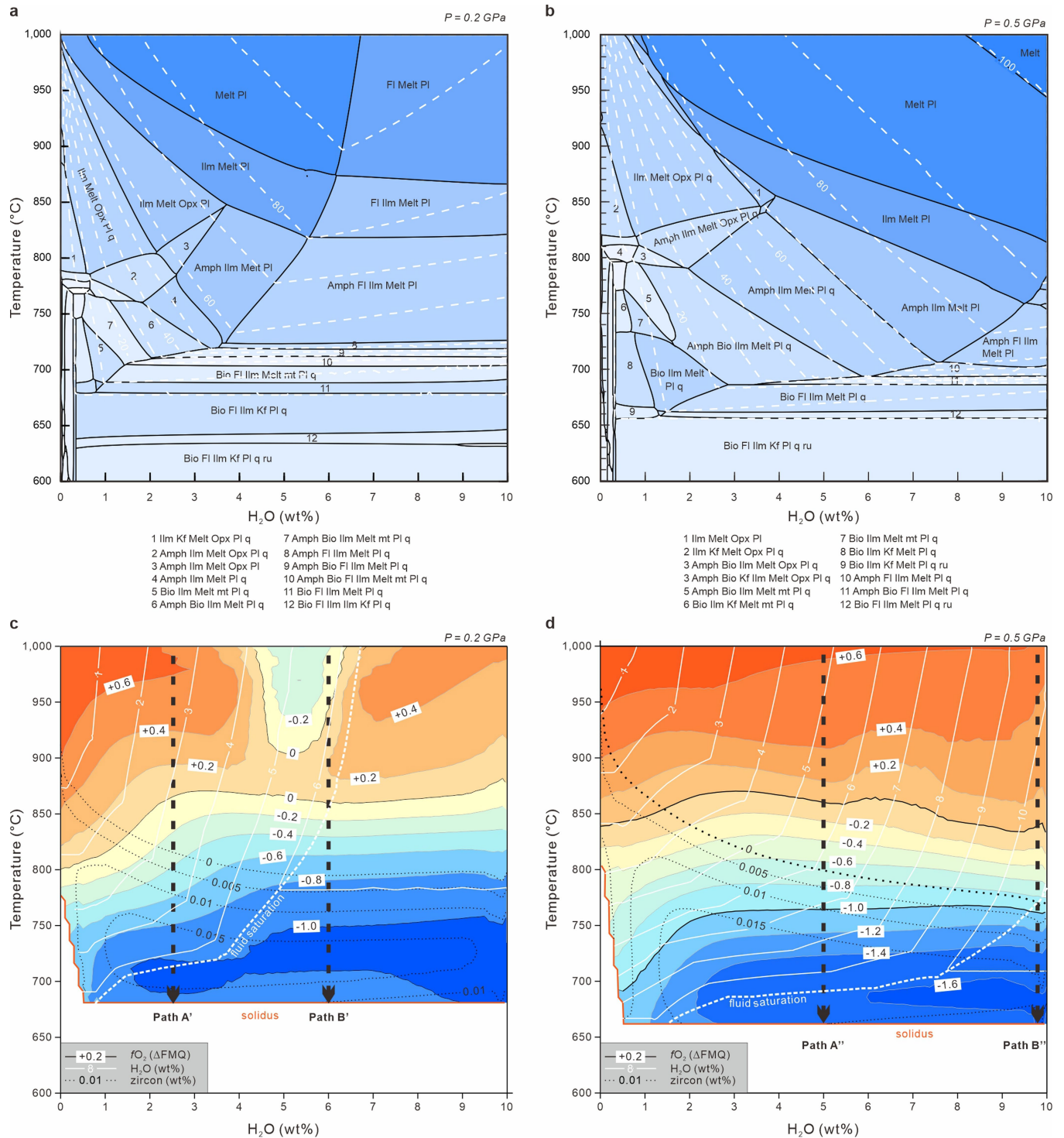
Extended Data Fig. 4 | Correlations of $f\text{O}_2$ and zircon Eu anomalies (Eu/Eu^*) with zircon Hf contents. **a**, The 3.72-Ga Aktash gneisses and the 3.2–3.0-Ga Heluositan gneisses of the Tarim Craton. **b**, The 4.02–2.95-Ga Acasta gneisses. **c**, The Toba Tuff (about 0.07 million years ago) and the Pea Ridge rhyolite (about 1,450 million years ago). The negative correlations between ΔFMQ and zircon Hf contents in the Archaean TTGs (**a,b**) suggest that, with crystallization of the magma, as indicated by increasing Hf in the residual melt and therefore

crystallizing zircon, the magmatic $f\text{O}_2$ decreases, owing to crystallization of amphibole and ilmenite that have slightly higher $\text{Fe}^{3+}/\Sigma\text{Fe}$ ratios than the primary TTG melts with relatively low $\text{Fe}^{3+}/\Sigma\text{Fe}$ ratios. This implies that the median ΔFMQ values, and therefore the calculated magmatic H_2O contents, are probably minimum estimates of the primary TTG melts. The negative correlations between zircon Eu/Eu^* and Hf contents suggest that zircon co-crystallized with plagioclase.



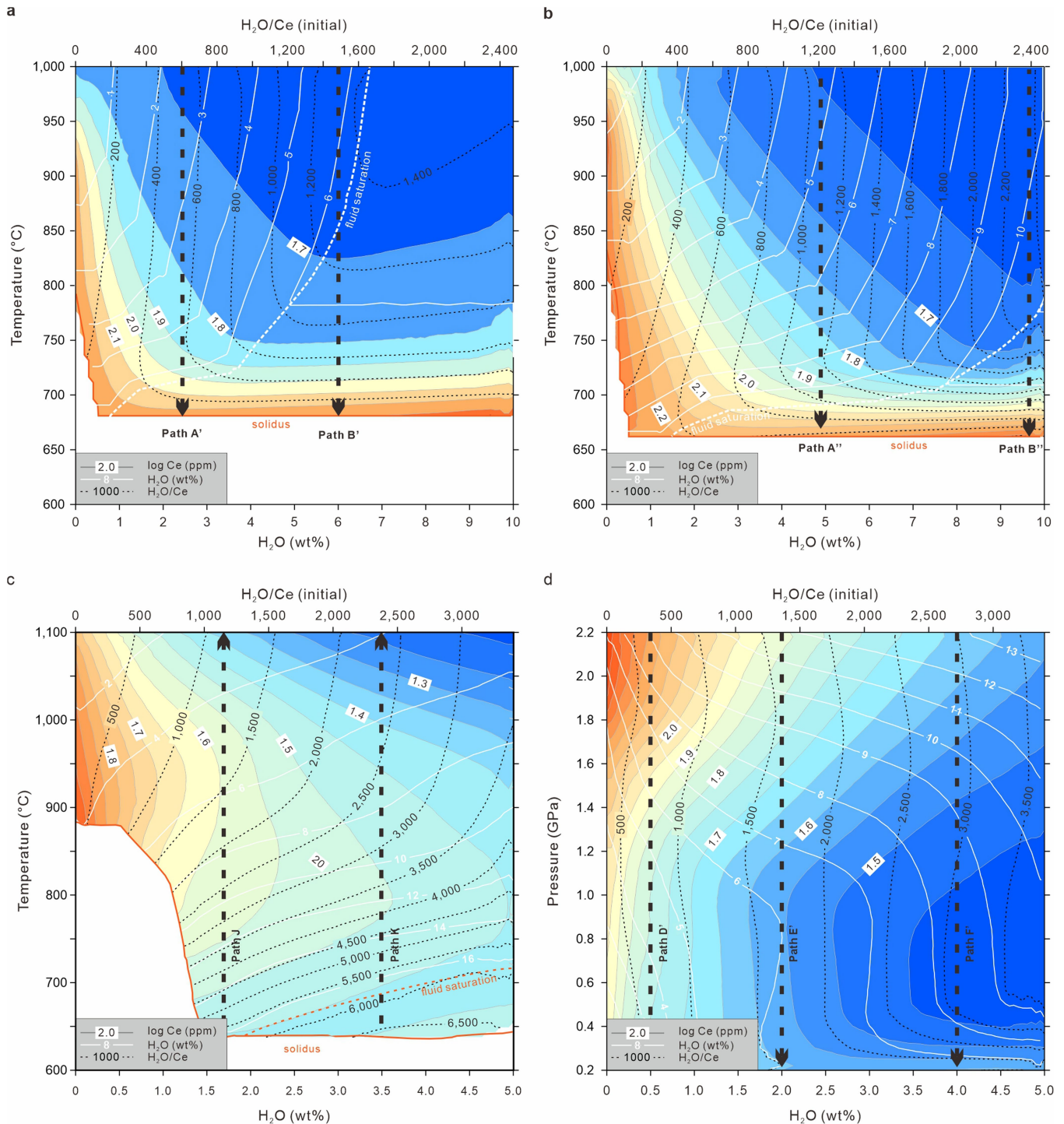
Extended Data Fig. 5 | Phase diagrams for Fig. 3. a, T -H₂O diagram for the median sodic TTG. P-T (b), P-H₂O (c) and P-fO₂ (d) diagrams for the median enriched Archaean basalt. These diagrams correspond to the isopleth diagrams in Fig. 3. The dashed white lines are melt isopleths in wt%.

Article



Extended Data Fig. 6 | Further T - H_2O diagrams and isopleth diagrams for the median sodic TTG. **a** and **b** correspond to the T - H_2O diagrams calculated at 0.2 and 0.5 GPa, respectively, assuming initial $\Delta\text{FMQ} = 0$ at 800°C , whereas **c** and **d** are the corresponding isopleth diagrams. In **c** and **d**, paths A' and A'' correspond to zircon crystallization in initially H_2O -undersaturated magmas

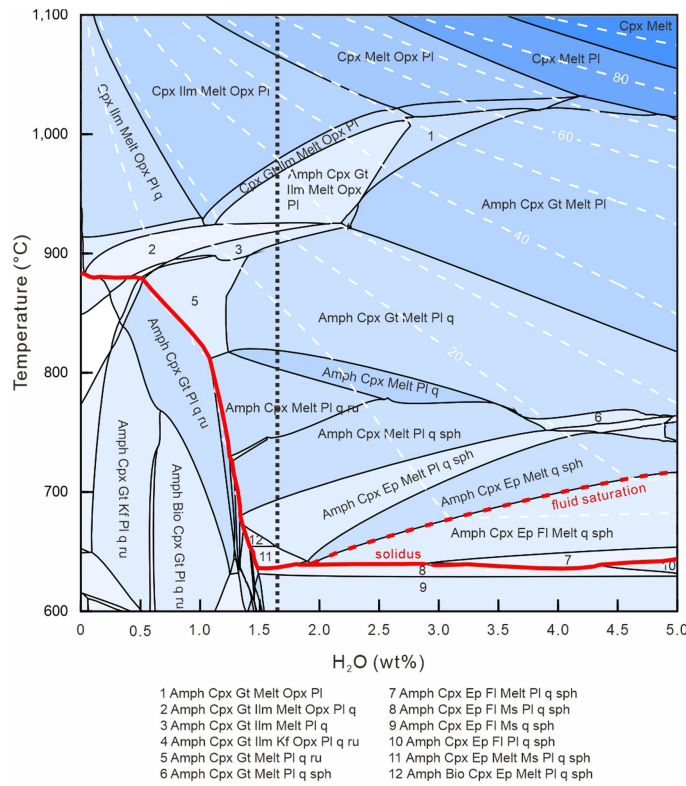
with lower H_2O content and predict a negative correlation between $f\text{O}_2$ and H_2O , which is not observed. By contrast, paths B' and B'' correspond to zircon crystallization in H_2O -saturated magmas at 0.2 and 0.5 GPa, respectively, and can explain the observed magmatic H_2O content of about 6 wt% and about 10 wt% in most Archaean granitoids.



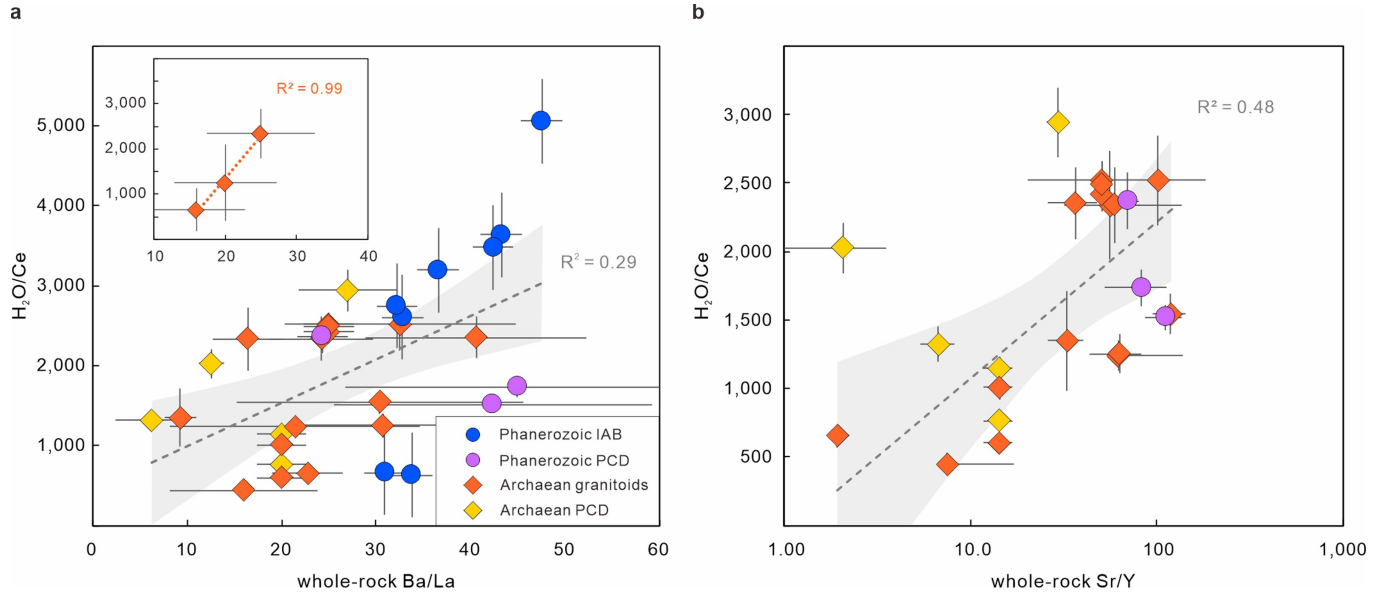
Extended Data Fig. 7 | The $\text{H}_2\text{O}/\text{Ce}$ systematics during the crystallization and formation of TTG melts. **a** and **b** correspond to the T - H_2O diagrams of the median sodic TTGs at about 0.2 and 0.5 GPa, respectively (Extended Data Fig. 6), whereas **c** and **d** correspond to the T - H_2O and P - H_2O diagrams of the median-enriched Archaean basalts, respectively (Extended Data Figs. 8 and 5d). The top abscissas show the initial $\text{H}_2\text{O}/\text{Ce}$ ratios of the system according to the model H_2O contents and Ce concentrations of the median sodic TTGs (40.4 ppm)¹⁵ and enriched Archaean basalts (14.7 ppm)³⁰. The colour scale shows the logarithm Ce concentrations in melts (in ppm), which are largely controlled by melt proportions (approximately $1/F$) because Ce is highly incompatible in major phases (LREE-rich accessory phases, for example, apatite and allanite, are not modelled). The solid white and dashed black lines are the isopleths of melt H_2O contents (wt%) and $\text{H}_2\text{O}/\text{Ce}$ ratios, respectively. **a** and **b** show that the melt $\text{H}_2\text{O}/\text{Ce}$ ratios did not change substantially during

the crystallization of TTG melts (paths A', A'', B' and B'') and correspond well with the initial $\text{H}_2\text{O}/\text{Ce}$ ratios, unless fluid saturation is reached when melt H_2O content is buffered by fluid and the melt $\text{H}_2\text{O}/\text{Ce}$ ratio becomes lower than the initial value. **c** and **d** show that the $\text{H}_2\text{O}/\text{Ce}$ ratios of TTG melts produced by isobaric heating (paths J and K) and isothermal decompression (paths D', E' and F') approach the initial $\text{H}_2\text{O}/\text{Ce}$ ratios of the magma sources, except at low-temperature (<900 $^{\circ}\text{C}$) conditions in which low-degree melting (or extreme fractionation) produces extremely H_2O -rich melts with high $\text{H}_2\text{O}/\text{Ce}$ ratios even from relatively H_2O -poor sources. However, this process is unlikely to generate large-scale TTG melts because the melt proportions are too low (<10 wt%). Instead, the high $\text{H}_2\text{O}/\text{Ce}$ ratios of the groups 2 and 3 Archaean TTGs can be explained by partial melting (or fractionation) of mafic sources with 1.5–2.0 and 3–4 wt% H_2O at ≥ 900 $^{\circ}\text{C}$ conditions, respectively.

Article



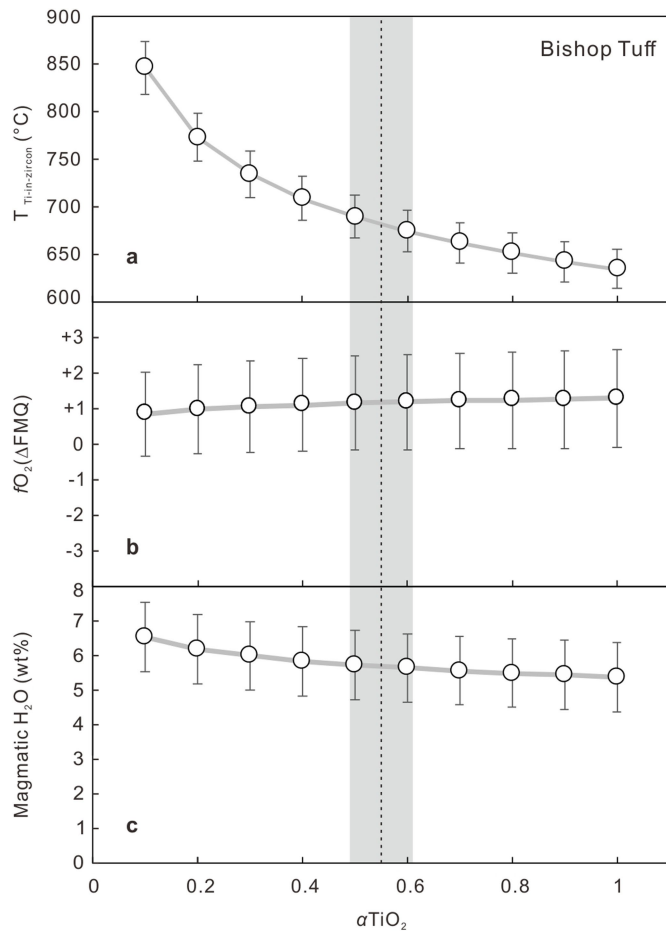
Extended Data Fig. 8 | T - H_2O diagram for the median-enriched Archaean basalt. This diagram is calculated at 1.1 GPa, at which the solidus temperature is the lowest (about 637°C). The thick red line shows the solidus, whereas the dashed red line corresponds to fluid saturation. The dotted black line shows the H_2O content used in the modelling in Fig. 3b,d, which slightly oversaturates the solidus at the lowest temperature. The dashed white lines show the melt isopleths in wt%.



Extended Data Fig. 9 | The correlations of $\text{H}_2\text{O}/\text{Ce}$ with Ba/La and Sr/Y ratios.

Archaean rocks. Data for Archaean granitoids (orange diamonds) and Phanerozoic and Archaean PCDs (purple circles and yellow diamonds, respectively) are from this study (Supplementary Table 3), whereas data for Phanerozoic IAB (blue circles) are from ref. 32. Error bars are 2 s.e.m. **a**, The positive correlation between $\text{H}_2\text{O}/\text{Ce}$ and Ba/La suggests that the magma sources of Archaean granitoids were variably influenced by influx of fluids, as in Phanerozoic arc magmas. The large variations in Ba/La ratios of Archaean granitoids probably result from metamorphic disturbance of whole-rock Ba, whereas the lower Ba/La and $\text{H}_2\text{O}/\text{Ce}$

ratios of Archaean rocks compared with Phanerozoic arc magmas probably suggest that Archaean subduction was less efficient in H_2O transport than Phanerozoic subduction. The dashed black line and shaded grey area are the linear regression and 95% confidence level for all data, respectively. The inset shows the distribution and correlation for the three groups of Archaean granitoids identified in the main text. **b**, The positive correlation between $\text{H}_2\text{O}/\text{Ce}$ and Sr/Y suggests that the H_2O -rich sources of Archaean TTGs occurred in the deep lower crust or the mantle. Symbols are the same as in **a**.



Extended Data Fig. 10 | The effects of varying αTiO_2 on Ti-in-zircon temperature, magmatic $f\text{O}_2$ and H_2O content. This is illustrated using zircon and melt inclusion data for the Ig2E unit of the Bishop Tuff. The vertical dashed line and grey bar show the αTiO_2 and standard error of the Bishop Tuff, according to the magnetite–ilmenite data¹². It is apparent that varying αTiO_2 values may introduce large (>50 °C) uncertainties in Ti-in-zircon temperature but do not notably affect the estimates of $f\text{O}_2$ (ΔFMQ) or H_2O content.